© 2020. Published by The Company of Biologists Ltd | Development (2020) 17, dev180042. doi:10.1242/dev.180042

RESEARCH ARTICLE

IRX3/5 regulate mitotic chromatid segregation and limb bud shape

Hirotaka Tao[1], Jean-Philippe Lambert[2,*], Theodora M. Yung[1], Min Zhu[3], Noah A. Hahn[1,4], Danyi Li[1,4], Kimberly Lau[1], Kendra Sturgeon[1], Vijitha Puviindran[1], Xiaoyun Zhang[1], Wuming Gong[5], Xiao Xiao Chen[4], Gregory Anderson[6], Daniel J. Garry[5], R. Mark Henkelman[6], Yu Sun[3], Angelo Iulianella[7], Yasuhiko Kawakami[8], Anne-Claude Gingras[2,4], Chi-chung Hui[1,4,‡] and Sevan Hopyan[1,4,9,‡]

ABSTRACT

Pattern formation is influenced by transcriptional regulation as well as by morphogenetic mechanisms that shape organ primordia, although factors that link these processes remain under-appreciated. Here we show that, apart from their established transcriptional roles in pattern formation, IRX3/5 help to shape the limb bud primordium by promoting the separation and intercalation of dividing mesodermal cells. Surprisingly, IRX3/5 are required for appropriate cell cycle progression and chromatid segregation during mitosis, possibly in a nontranscriptional manner. IRX3/5 associate with, promote the abundance of, and share overlapping functions with co-regulators of cell division such as the cohesin subunits SMC1, SMC3, NIPBL and CUX1. The findings imply that IRX3/5 coordinate early limb bud morphogenesis with skeletal pattern formation.

KEY WORDS: Iroquois, Cohesin, Limb development, Mesodermal cell intercalations, Mitotic chromatid segregation, Morphogenesis

INTRODUCTION

Iroquois (Irx) genes were first identified as regulators of pre-pattern that control specification of large territories during *Drosophila* development (Cavodeassi et al., 2001). They encode proteins of the TALE subclass of atypical homeodomains (Burglin, 1997; Cavodeassi et al., 2001), other members of which include the MEIS and PBX proteins that are characterised by three additional amino acid residues (proline-tyrosine-proline) between helix 1 and helix 2 (Burglin, 1997). In mice, six Irx genes are found in two clusters: IrxA cluster contains *Irx1*, *Irx2* and *Irx4*, and IrxB cluster consists of *Irx3*, *Irx5* and *Irx6* (Gómez-Skarmeta and Modolell, 2002).

[1]Program in Developmental and Stem Cell Biology, Research Institute, The Hospital for Sick Children, Toronto, ON M5G 1X8, Canada. [2]Lunenfeld-Tanenbaum Research Institute, Sinai Health System, Toronto, ON M5G 1X5, Canada. [3]Department of Mechanical and Industrial Engineering, University of Toronto, ON M5S 3G8, Canada. [4]Department of Molecular Genetics, University of Toronto, Toronto, ON M5S 1A8, Canada. [5]Lillehei Heart Institute, University of Minnesota, Minneapolis, MN 55455, USA. [6]Mouse Imaging Centre, Hospital for Sick Children, Toronto Centre for Phenogenomics, Department of Medical Biophysics, University of Toronto, Toronto, ON M5T 3H7, Canada. [7]Department of Medical Neuroscience, Dalhousie University, Halifax, NS B3H 4R2, Canada. [8]Department of Genetics, Cell Biology and Development, Stem Cell Institute, University of Minnesota, Minneapolis, MN 55455, USA. [9]Division of Orthopaedic Surgery, Hospital for Sick Children and University of Toronto, Toronto M5G 1X8, Canada.
*Present address: Department of Molecular Medicine, Université Laval, CHU de Québec-Université Laval Research Centre, Québec, PQ G1V 4G2, Canada.

‡Authors for correspondence (sevan.hopyan@sickkids.ca; cchui@sickkids.ca)

J.-P.L., 0000-0002-0833-1221; N.A.H., 0000-0003-4374-3368; W.G., 0000-0002-3147-4028; C.-c.H., 0000-0001-7047-6694; S.H., 0000-0001-7201-8902

Handling Editor: Benoit Bruneau
Received 30 April 2019; Accepted 25 August 2020

IRX proteins are recognised for their ability to activate and repress transcription in a wide variety of developmental and physiological contexts (Costantini et al., 2005; Lee et al., 2004; Matsumoto et al., 2004; Kim et al., 2012; Bilioni et al., 2005). *Irx3* is a target of obesity-associated variants within the *FTO* locus (Smemo et al., 2014) and regulates cardiac conduction (Zhang et al., 2011). *Irx5* influences terminal differentiation of retinal bipolar neurons (Cheng et al., 2005) and of cardiomyocytes (Costantini et al., 2005). *Irx3* and *Irx5* are located about 550 kb apart on mouse chromosome 8 and are expressed in overlapping domains in the developing heart and limb, in which they have partially redundant functions (Gaborit et al., 2012; Li et al., 2014).

In the developing limb, anteroposterior polarity of the early bud is essential for the formation of appropriate skeletal pattern and is marked by domains of anterior *Gli3* and posterior *Hand2* expression (Te Welscher et al., 2002; Zhulyn et al., 2014; Tao et al., 2017). *Irx3*/*5* are required for the expression of anterior mesodermal markers and for the formation of proximal (femur) and anterior (tibia, first and second rays) skeletal elements, specifically in the hindlimb. *Irx3*/*5* counterbalance the posterior pattern regulator sonic hedgehog (*Shh*) that is downstream of *Hand2*, by directly upregulating transcription of the hedgehog antagonist *Gli3*. Hindlimb specificity of the mutant phenotype may be attributable to the greater *Gli3*-rich anterior domain in the forelimb that protects against diminished expression due to *Irx3*/*5* deficiency. Interestingly, *Irx3*/*5* are required during limb initiation before there is molecular evidence of emergent skeletal pattern (Li et al., 2014; Zhulyn et al., 2014). At that early stage, the *Irx3*/*5* mutant limb bud is deformed and has apparently diminished anterior mesodermal volume, although it is unclear what cellular functions are affected.

Some of the key cell behaviours that are known to underlie early limb bud morphogenesis include directional mesenchymal cell movements and oriented cell divisions (Boehm et al., 2010; Gros et al., 2010; Wyngaarden et al., 2010; Mao et al., 2015). For limb bud ectoderm, the immediate intercalation of daughter cells among neighbouring cells is an important process that precipitates cell rearrangements to orient tissue growth (Lau et al., 2015). The separation of daughter cells, or cytokinesis, involves well defined changes in cellular morphology that include remodelling of the cortex, constriction of a cleavage furrow, and severing, or abscission, of the plasma membrane (Mohan et al., 2012; Liu and Robinson, 2018). During this process, sister chromatids are separated and any lagging chromosomes must be cleared (Morales and Losada, 2018; Liu and Robinson, 2018). Although specific pathways such as the NoCut checkpoint control that process (Mendoza et al., 2009), the loss of function of various proteins and complexes disrupts sister chromatid segregation and results in chromosome bridge formation at anaphase that delays or prevents cytokinesis. Cohesin and condensin complexes that are composed

Development (2020) 17, dev180042. doi:10.1242/dev.180042

of structural maintenance of chromosomes (SMC1A/3, SMC2/4, respectively) family proteins (DeMare et al., 2013; Jeppsson et al., 2014; Kschonsak and Haering, 2015) are responsible for the establishment of interphase chromatin structure and the formation of condensed chromosomes in mitosis (Kakui and Uhlmann, 2018). The cohesin complex regulates embryonic development in plants and animals by pairing sister chromatids during cell division and by influencing transcription (Minina et al., 2017; Smith et al., 2014; Marsman et al., 2014; Tedeschi et al., 2013; Mouri et al., 2012; Kawauchi et al., 2009). During S phase, replicated sister chromatids are connected with one another by the monomeric ring-like cohesin complex, and this cohesion is necessary for biorientation and orderly segregation of chromosomes on the mitotic spindle (Peters and Nishiyama, 2012; Skibbens, 2008; Liu et al., 2019). Interestingly, deficiency of nipped-B-like (*Nipbl*), the product of which facilitates cohesin loading (Hirano, 2006), results in fin bud undergrowth and transcriptional misregulation in the mouse limb bud (Muto et al., 2014), as well as tibial deficiency that is a feature in common with human cohesinopathies (Pfeiffer and Correll, 1993) and murine *Irx3/5* deletion (Li et al., 2014). Knockdown of other, seemingly unrelated, proteins such as the CUX1 homeodomain protein and the KIFC1 kinesin also results in chromosome bridge formation (Sansregret et al., 2011; Kim and Song, 2013), underscoring the apparent complexity of the final stages of cell division.

Here, we show that mesodermal cells in the mouse limb bud intercalate among their neighbours immediately after cell division. IRX3/5 are required for consistent daughter cell separations and intercalations that shape the limb bud. Unexpectedly, IRX3/5 are required for mitotic chromatid separation specifically in the anterior region of the limb bud. IRX3/5 are in close proximity to cohesin subunits and CUX1 and promote their abundance in that region. These data suggest that IRX3/5 share overlapping functions with regulators of cell division and contribute to early limb bud morphogenesis in addition to their recognised role in skeletal pattern formation.

RESULTS

Irx3/5 regulate limb bud morphogenesis and mesodermal daughter cell intercalation

To assess early limb bud morphology in the mouse embryo, we employed optical projection tomography (OPT). *Irx3/5*$^{-/-}$ mutant hindlimb buds were short and bulbous relative to those of wild-type (WT) littermates owing to disproportionate undergrowth of their anteroposterior (AP) and proximodistal (PD) axes and overgrowth of their dorsoventral (DV) axes between somite stages (som.) 31 and 37 (Fig. 1A-D, Movies 1 and 2). Previously, we have shown that oriented cell motility and division are important for early limb bud morphology (Wyngaarden et al., 2010). To examine dynamic cell behaviours that might underlie this dysmorphology, we performed live time-lapse light sheet imaging of intact mouse embryos that harbour an H2B-GFP transgene (Hadjantonakis and Papaioannou, 2004) for 2.5 h periods at som. 32 stage (Movies 3 and 4). Limb bud mesodermal cell tracks in 3D (documented using Imaris, Movies 5 and 6) were converted to cell displacements using particle image velocimetry in Matlab (Movies 7 and 8) to generate 3D 'dandelion' plots for analysis. In contrast to the predominantly distalward displacement of mesodermal cells in the WT background, H2B-GFP; *Irx3/5*$^{-/-}$ mutant cells moved more radially (Fig. 1E,F, Movies 9 and 10), and these movements are qualitatively consistent with the relatively bulbous shape of the mutant bud. To assess the longer-term consequences of cell movement differences, we activated the transgenic multi-colour reporter Confetti (Snippert et al., 2010) using tamoxifen-responsive Esr1:Cre (Lee et al., 2014) to facilitate the identification of changes in cellular position over time. Approximately 24 h after tamoxifen delivery, these embryos were harvested and wide-field confocal analysis of the entire 29-30 som. hindlimb field was performed before and after 8 h in aerated roller culture supplemented with rat serum. Overall mesodermal cell displacements were diminished in *Irx3/5*$^{-/-}$ mutants (Fig. S1A-D), suggesting that mechanisms of cell movement were impaired (labelling of cells with Confetti was random as no distinct population was reproducibly labelled in different experiments, and variation of tamoxifen dose did not systematically affect the labelled population; Fig. S1E). These observations imply that dysmorphology in the *Irx3/5*$^{-/-}$ mutants is attributable to disoriented and diminished mesodermal cell displacements in developing limb buds.

To more precisely define dynamic mesodermal cell behaviours, we examined Esr1:Cre;Confetti transgenic embryos at higher resolution. During confocal live imaging of an anterior hindlimb field of ∼150 mesodermal cells through 20 frames at 5 min intervals, WT daughter cells frequently separated from one another and intercalated among their neighbours immediately following cell division. In contrast, *Irx3/5*$^{-/-}$ mutant daughter cells more often remained adjacent to one another and failed to intercalate among neighbouring cells (Fig. 1G,H, Movies 11 and 12). Daughter cell intercalation contributes to reshaping limb bud ectoderm (Lau et al., 2015), and these observations suggest that *Irx3/5* facilitate the same process in limb bud mesoderm, possibly by affecting cell division or daughter cell separation.

To ask whether cell division is affected by *Irx3/5*, we measured cell cycle time *in vivo* by assessing the proportion of cells that exited S phase between timed CidU and IddU injections of pregnant females as described previously (Boehm et al., 2010) (Fig. S2A). Consistent with the anterior domain of *Irx3/5* expression (Li et al., 2014), cell cycle time was lengthened (11.3 versus 9.7 h) in anterior, but not posterior (10.2 versus 10.2 h), mesoderm of mutant 29 som. hindlimb buds (Fig. 2A). These cell cycle times are at the short end of the range documented previously for the later stage embryonic day (E) 11.0-11.25 forelimb bud (Boehm et al., 2010), suggesting mesodermal cell division slows during development. Flow cytometry of DAPI-stained cells that we dissociated from limb buds demonstrated that 21.3% of mutant cells were in G2/M phase compared with 13.4% for WT (Fig. 2B), implying that mitotic transit was delayed in mutant embryonic cells.

To seek further insight into the source of mitotic delay and lack of daughter cell separation that we had observed, we analysed mitotic cells in live *H2B-GFP* reporter embryo movies. To our surprise, 61.5% of mitotic cells in the anterior hindlimb mesoderm of 27-29 som. *Irx3/5*$^{-/-}$ mutant embryos (versus 9.5% in WT) exhibited chromatin bridges during the metaphase-to-anaphase transition (Fig. 2C, Movies 13-16). Chromatin bridges resulted in one of three primary outcomes. Some bridges resolved after a delay and allowed for clear chromatid separation (that we defined as a lagging chromosomal bridge; Movie 14). Some bridges persisted until chromatin decondensation was apparent at the beginning of interphase, resulting in failure of daughter cell separation, or until chromatin fragmentation was apparent (that we defined as a persistent bridge; Movie 15). Complete failure of metaphase chromatin separation was also noted in a small proportion of cases (Fig. 2D, Movie 16). We documented the duration of mitotic phases that were clearly observable using the H2B-GFP reporter for live imaging *in vivo*. Among *Irx3/5*$^{-/-}$ mutant mesodermal cells, the metaphase-telophase transition period was extended, and a greater proportion of those in telophase subsequently exhibited chromatin fragmentation

Development (2020) 17, dev180042. doi:10.1242/dev.180042

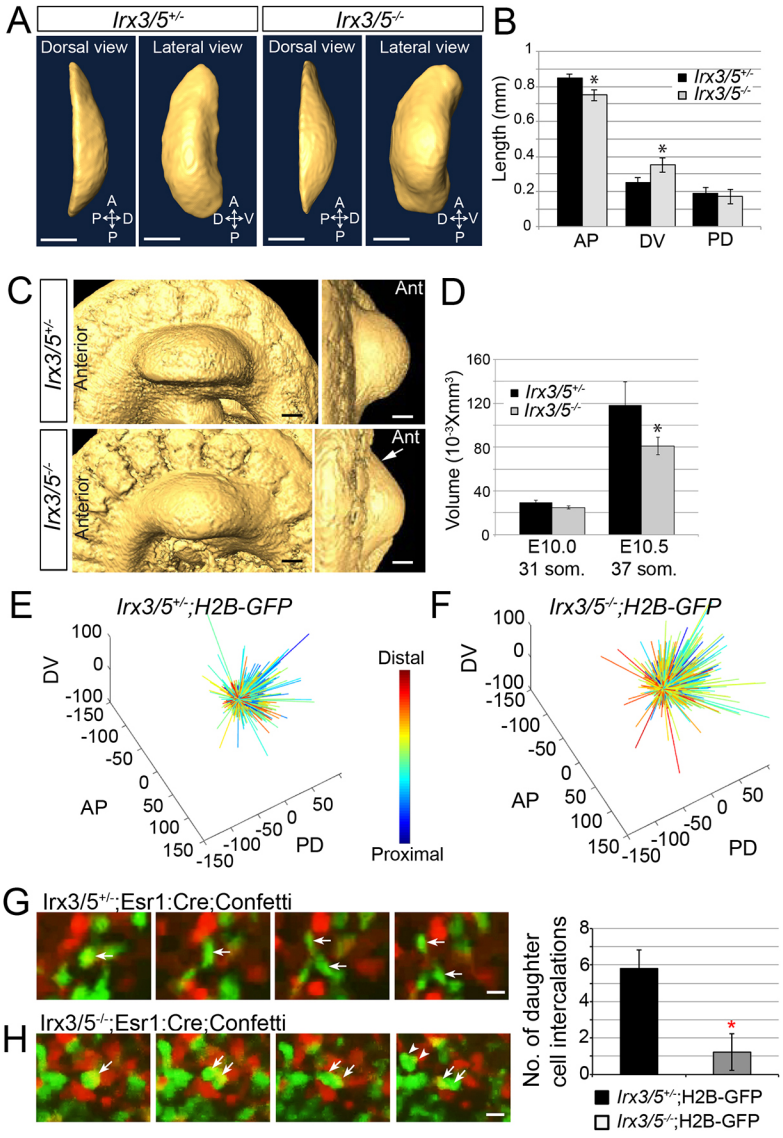

Fig. 1. *Irx3/5* regulate limb bud shape and daughter cell intercalation. (A,B) OPT images (A) and axis lengths (B) of *Irx3/5*$^{+/-}$ (WT) and *Irx3/5*$^{-/-}$ early hindlimb buds at 31 som. (n=3 embryos, six hindlimb buds). AP, *P=0.032; DV, *P=0.021 (unpaired, two-tailed Student's t-test based on n=3) (C) OPT images of *Irx3/5*$^{+/-}$ and *Irx3/5*$^{-/-}$ limb buds at 37 som. Arrow indicates anterior region that was increasingly deficient among *Irx3/5*$^{-/-}$ mutants. (D) Volume of *Irx3/5*$^{+/-}$ and *Irx3/5*$^{-/-}$ limb buds (for 31 and 37 som., n=3 embryos per condition, *P=0.013, unpaired, two-tailed t-test). (E,F) Dandelion plots show 3D displacement of hindlimb mesodermal cells in 32 som. WT (*Irx3/5*$^{+/-}$, E) and *Irx3/5*$^{-/-}$ mutant (F) embryos during live light sheet imaging (n=3 per condition). (G,H) Live confocal imaging from within a 150 mesodermal cell field within the anterior hindlimb of Esr1:Cre;Confetti embryos revealed intercalation of *Irx3/5*$^{+/-}$ nascent daughter cells (arrows) among their cell neighbours during a 100 min session at 5 min intervals (29-30 som., n=3 embryos) (G). In contrast, *Irx3/5*$^{-/-}$ mutant daughter cells failed to separate and intercalate (H) (29-32 som., n=3 embryos, *P=0.003, t-test). AP, anteroposterior; DV, dorsoventral; PD, proximodistal. Scale bars: 200 µm (A,C); 20 µm (G,H).

instead of transitioning to interphase (Fig. S2B, Movie 17). Therefore, *Irx3/5* regulate mitotic progression by promoting chromatid segregation.

Time-lapse evidence of daughter cell fragmentation suggested that the fate of dividing cells with persistent chromatin bridges was apoptosis. We have previously shown that apoptotic cells were more numerous in the *Irx3/5*$^{-/-}$ mutant anterior hindlimb bud by 37 som. (Li et al., 2014), but we did not clearly identify a difference among caspase 3-positive cells at 29 som. (Fig. S2C) despite evident dysmorphology at that stage. It is uncertain whether the proportion of apoptotic cells is attributable entirely to failed mitoses, as we cannot directly compare the period of time represented by our time-lapse movies with our immunostains. Mutant mesodermal cells that did complete cytokinesis (a group that includes normal division and lagging chromosomes) exhibited disoriented planes of division (Fig. 2E). Not surprisingly, these findings underscore the importance of chromatid segregation for morphogenesis.

IRX3/5 bind with regulators of chromatid segregation

To test whether *Irx3/5* regulate the transcription of genes that promote chromatid segregation, we performed RNA-seq of whole tissue posterior to somite 20 that includes the hindlimb fields of 26/27 som. *Irx3/5*$^{-/-}$ mutant embryos. Relative to WT specimens, *Irx3/5*$^{-/-}$ mutants exhibited significant changes in the expression of many genes including those that regulate translation, fatty acid β-oxidation, megakaryocyte differentiation and hematopoietic progenitor cell differentiation. However, the expression of genes that regulate chromatid segregation or cell cycle progression was not significantly altered in mutants (Fig. S3, Table S1), raising the possibility that IRX3/5 regulate cell division in a nontranscriptional manner. NCBI BioSample accession numbers to the full RNA-seq dataset are noted in Table S2.

To identify proteins that associate with IRX3 and IRX5 in an unbiased fashion, we performed proximity-dependent biotin identification (BioID) coupled to mass spectrometry, a method that captures proximate (within 10 nm) and interacting proteins in living cells (Roux et al., 2012; Kim et al., 2014). HEK 293 cells were chosen based on our experience with them for BioID. Although these cells are not a developmental model, we note they express transcription factors that are important for establishing limb pattern at an early stage which is the focus of our study, such as *Gli2*, *Gli3* (Mo et al., 1997; Zhulyn et al., 2014), *Meis1*, *Meis2* (Mercader et al., 1999; Capdevila et al., 1999) and *Sall1-3* (Kawakami et al., 2009) according to proteinatlas.org and proteomicsdb.org. As expected, based on the

Development (2020) 17, dev180042. doi:10.1242/dev.180042

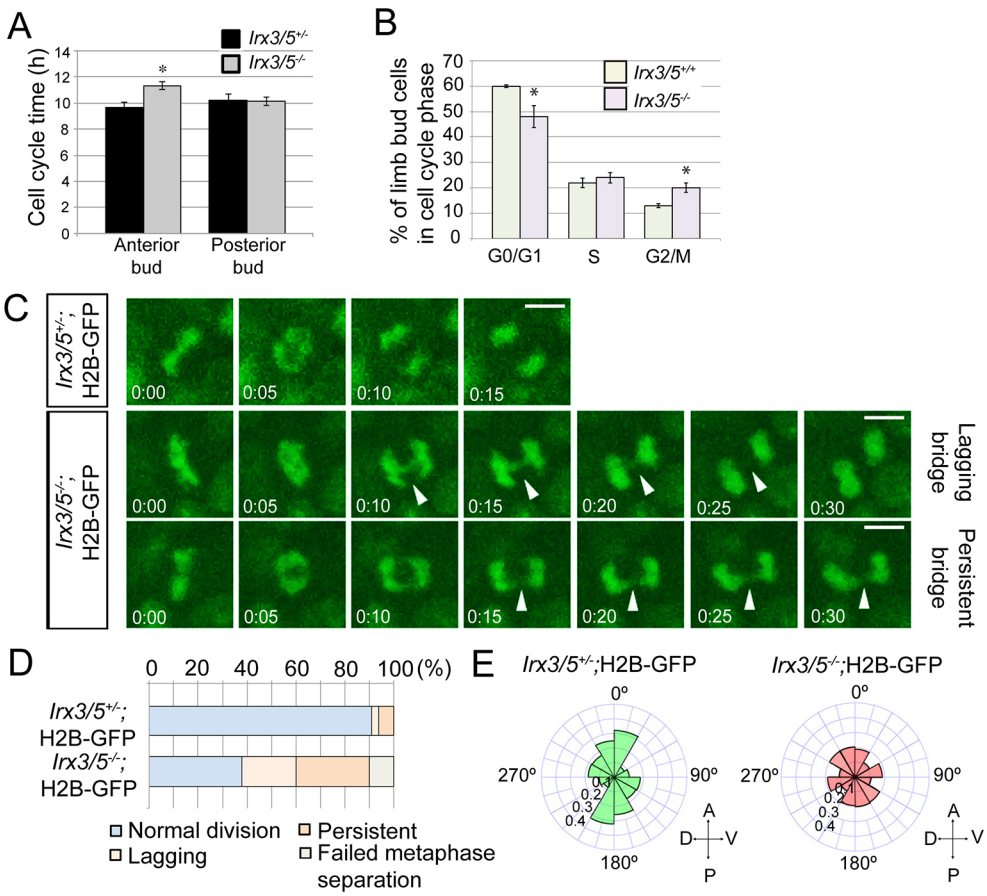

Fig. 2. *Irx3/5* regulate cell cycle progression and mitotic chromatid segregation. (A) Cell cycle time was lengthened in *Irx3/5*$^{-/-}$ mutant embryonic anterior mesoderm by CidU/IddU double labelling (28-29 som., for Irx3/5$^{+/-}$ *n*=5, for Irx3/5$^{-/-}$ *n*=4 embryos, **P*=0.018, unpaired, two-tailed *t*-test). (B) DNA content analysis by flow cytometry to estimate the proportion of limb bud cells within each cell cycle phase (*n*=3 embryos per condition G0/G1, **P*=0.008; G2/M, **P*=0.012, unpaired, two-tailed *t*-test). (C,D) Representative images (C) and quantification (D) of mesodermal cells in the anterior limb bud exhibiting a greater number of chromatin bridges in *Irx3/5*$^{-/-}$ mutants. For *Irx3/5*$^{+/-}$*;H2B-GFP*: normal division, 90.5%; lagging (temporary) bridge, 2.5%; persistent (permanent) bridge, 7.0%; complete failure of metaphase separation, 0%. For *Irx3/5*$^{-/-}$*; H2B-GFP*: normal division, 38.5%; lagging bridge, 21.5%; persistent bridge, 30%; complete failure of metaphase separation, 10% (29-30 som., *n*=4 embryos per condition). Arrowheads indicate anaphase bridge in anterior limb bud mesoderm. (E) Cell division planes were disoriented in anterior *Irx3/5*$^{-/-}$ mutant limb bud mesoderm (30-35 cell divisions, *n*=3 embryos per condition, 29-30 som.). Scale bars: 10 µm. Error bars indicate s.e.m.

known function of IRX3/5, multiple regulators of transcription that bind to DNA or to other transcription factors, including TLE, BCOR, ZNF, FOX and TCF, were among the highest probability neighbours of IRX3 and IRX5 in HEK 293 cells (Fig. 3A). Among these transcription factors were well-recognised regulators of limb development, such as DLX6, PITX1 and 5′ HOX proteins (Fig. 3B).

Given the cell cycle progression defects among *Irx3/5* deficient cells, we scrutinised BioID partners of IRX3/5 that regulate cell division. Two high significance IRX3/5 binding partners observed at a false discovery rate of less than 1% were the CUX1 homeodomain protein and the KIFC1 kinesin, which share a common cell division phenotype as knock down of either results in chromatin bridge formation (Sansregret et al., 2011; Kim and Song, 2013). Multiple subunits of the cohesin and condensin complexes, including SMC1A/3 and SMC2/4, NIPBL and multiple NCAPD/G proteins that regulate condensin (Seipold et al., 2009), were also identified at lower abundance in the BioID assay primarily of IRX3 (Fig. 3B). To help place these data into a context based on previously published observations, we employed a software tool called GeneMANIA (Warde-Farley et al., 2010) to predict interactions. That algorithm predicted physical interactions between IRX3/5 and several of our BioID hits, including cohesin subunits and CUX1 (Fig. 3C). Although the latter is not commonly regarded as sharing function with cohesin, their mutant phenotypes and co-enrichment in this assay suggested the possibility of overlapping functions in concert with IRX3/5. We therefore elected to focus further on cohesin and CUX1.

To test the BioID results and *in silico* predictions, we expressed full-length *Irx3* in HEK 293 cells. Anti-IRX3 antibody co-immunoprecipitated endogenous SMC1 (anti-SMC1 antibody recognises both SMC1a and SMC1b proteins) and CUX1 (Fig. S4A), supporting the binding of these proteins *in vitro*. To extend these analyses *in vivo*, we dissected and lysed 30 WT hindlimb buds. Under endogenous conditions, anti-IRX3 antibody co-immunoprecipitated SMC1, SMC3 and CUX1 (Fig. 4A). To study the spatial distribution of these proteins, we performed whole-mount and section immunostaining and identified IRX3 protein in mesodermal nuclei of the anterior-proximal limb bud in *Irx3/5*$^{+/-}$, but not *Irx3/5*$^{-/-}$, embryos by confocal microscopy as expected. Similar to the domain of *Irx3* mRNA (Li et al., 2014), IRX3 protein was absent in the posterior-distal limb bud (Fig. 4B). To visualise proteins of interest at higher resolution, we employed stimulated emission depletion (STED) microscopy (Fornasiero and Opazo, 2015). In anterior limb bud mesoderm, IRX3 appeared as distinct puncta that were in close proximity to SMC1 or CUX1 such that no gap between those pairs could be resolved by STED, a situation we referred to as contacts (Fig. 4C). To test whether those endogenous proteins were physically bound *in vivo*, we used the proximity ligation assay (PLA), a method that detects protein-protein interactions with high specificity (Ke et al., 2013). IRX3 associated with SMC1 in 9.7% and with CUX1 in 12.5% of anterior mesodermal hindlimb nuclei (Fig. 4D,E). We interpret these findings to imply that IRX3 physically interacts with SMC1 and CUX1 in an intermittent fashion.

Irx3/5 promotes cohesin subunit and CUX1 protein abundance

We asked whether the presence of *Irx3/5* impacted cohesin subunits and CUX1. Immunostain intensities of SMC1, SMC3, NIPBL and CUX1 were diminished specifically in anterior hindlimb mesoderm in *Irx3/5*$^{-/-}$ mutants *in vivo* relative to WT controls (Fig. 5A-C,

Development (2020) 17, dev180042. doi:10.1242/dev.180042

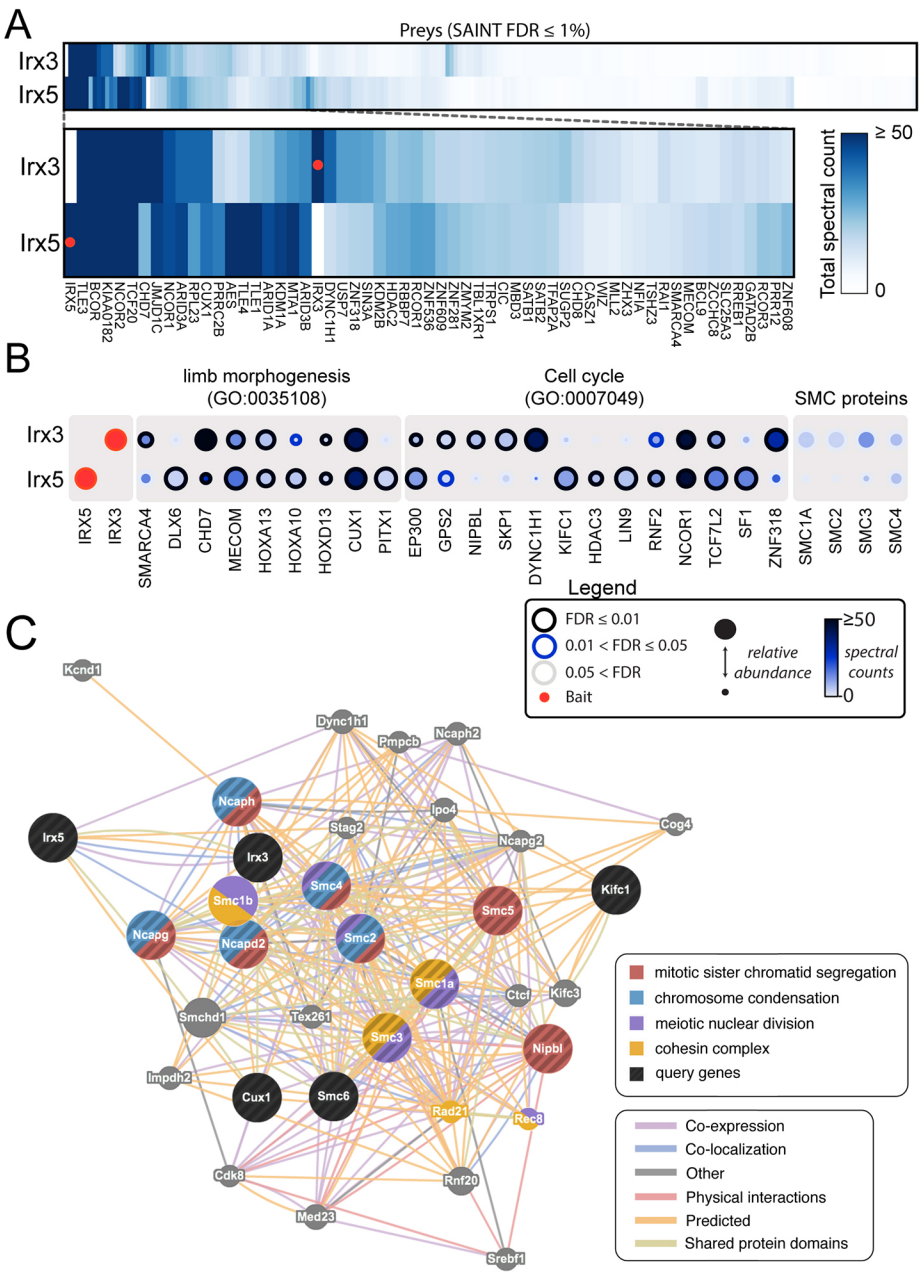

Fig. 3. IRX3/5 protein partners by BioID. (A) Heat map of the total spectral count observed for each significant prey [SAINT; false discovery rate (FDR) ≤1%] identified by BioID. Highlights of results are provided in bottom panel. (B) Dot plot representation of selected preys identified with IRX3 and IRX5 by BioID associated with limb morphogenesis (GO term 0035108) and cell cycle (GO term 0007049). (C) Connectivity diagrams from GeneMANIA (http://www.genemania.org) showing potential physical interactions among IRX3, IRX5 and proteins isolated from BioID data.

Fig. S5). We note that delayed mitosis could result in some of the SMC1 depletion that we observed in mutants, as SMC1 is removed from chromosome arms during mitosis (Waizenegger et al., 2000; Sumara et al., 2000). Consistent with our RNA-seq data, RT-quantitative PCR of tissue dissected from the anterior hindlimb indicated that transcription of the *Smc1a*, *Smc1b* and *Cux1* genes was unaltered in *Irx3/5*$^{-/-}$ mutants (Fig. 5D,E). Therefore, *Irx3/5* contribute to the abundance of at least some cohesin subunits and CUX1 in a regional, and likely nontranscriptional, fashion.

Irx3/5 exhibit overlapping function with *Cux1/2*

The preceding datasets suggest that IRX3/5 have overlapping functions and might cooperate with cohesin and CUX1 to promote regionally appropriate cell division. To further address this possibility, we asked whether removal of *Cux1/2* results in a limb bud phenotype that resembles that of *Irx3/5*$^{-/-}$ mutants. Although *Cux1* is widely expressed, *Cux2* is restricted to the interlimb lateral plate and anterior aspect of the early hindlimb field (Iulianella et al., 2003). We crossed *Cux1*$^{+/-}$ (Luong et al., 2002) and *Cux2*$^{+/-}$ (Iulianella et al., 2008) mutants and observed that single homozygous and double heterozygous *Cux1/2* mutants did not exhibit a limb bud phenotype. Double homozygous *Cux1/2*$^{-/-}$ stage-matched 29 and 32 som. hindlimb buds were small with shortened PD axes that was most pronounced in the anterior region and resembled those of *Irx3/5*$^{-/-}$ mutants (Fig. 6A). The DV axis is broader in *Irx3/5* mutants, suggesting these regulators have overlapping but distinct morphogenetic functions. As with *Irx3/5*$^{-/-}$ mutants, the forelimb buds of *Cux1/2*$^{-/-}$ mutants were not affected (not shown), the proportion of pHH3-positive cells was diminished (Fig. S6A), and caspase 3-positive cells were rare (Fig. S6B). Interestingly, chromatin bridges were evident among *Cux1/2*$^{-/-}$ mutant mesodermal cells, although their fates could not be followed owing to the static nature of this analysis (Fig. 6B). Moreover, intensities of SMC1 and NIPBL immunostaining were

Development (2020) 17, dev180042. doi:10.1242/dev.180042

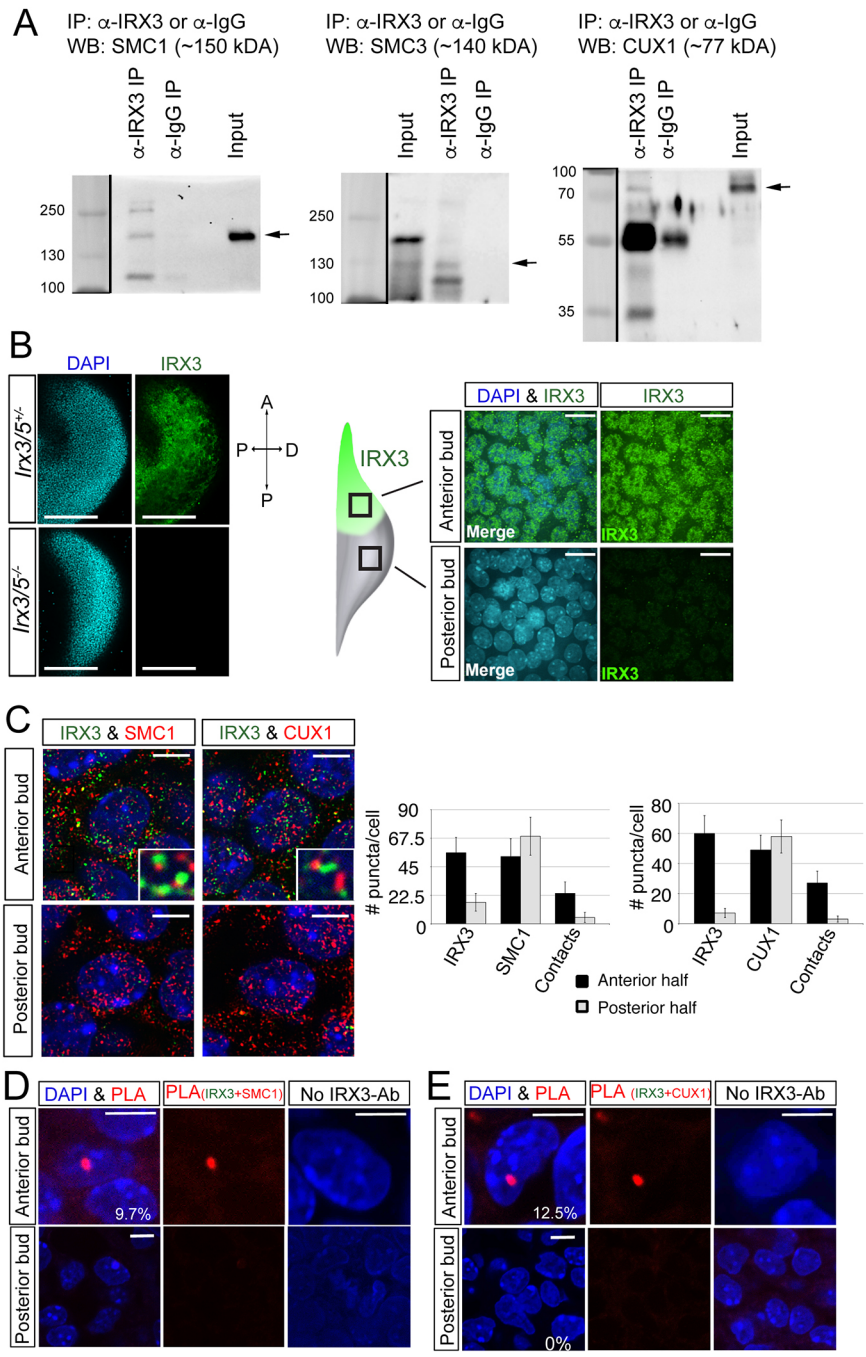

Fig. 4. IRX3 associates with SMC1 and CUX1 *in vivo*. (A) Lysate from 30 WT E10.5 hindlimb buds was immunoprecipitated (IP) with anti-IRX3 and immunoblotted against SMC1, SMC3 or CUX1. Three separate co-IP experiments were performed using multiple limb buds on each occasion. Representative full-length western blots (WB) are shown, and arrows indicate expected band size. (B) IRX3 protein localised in anterior-proximal (AP), but not posterior-distal (PD), nuclei in mesoderm of 29 som. limb bud. (C) STED microscopy revealed that IRX3 puncta contacted those of SMC1 (anterior versus posterior, P=0.008) and CUX1 (anterior versus posterior, P=0.005) in anterior mesoderm of the hindlimb field at 29-32 som. (25-30 cells, n=3 embryos, unpaired, two-tailed t-test, error bars indicate s.e.m.). (D,E) PLA *in vivo* demonstrated physical association of IRX3 with SMC1 (8/82, 9.7%; D) and CUX1 (8/64, 12.5%; E) in anterior half mesoderm at 29-30 som. (n=3 embryos per condition). Scale bars: 400 µm (B, left); 20 µm (B, right); 5 µm (C-E).

diminished specifically in the anterior region of the hindlimb bud (Fig. 6C). At later stages, limb shape and skeletal pattern were normal in E13.5 and E14.5 *Cux1/2*$^{-/-}$ mutants (Fig. S6C), implying the early morphogenetic deficiency had recovered. These data indicate that *Irx3/5* and *Cux1/2* have overlapping, though not necessarily interactive, morphogenetic functions in the early limb bud. Skeletal pattern, however, is regulated separately by *Irx3/5*.

DISCUSSION

The use of an unbiased protein binding assay and with live imaging were keys to identifying unexpected partners and processes regulated by IRX3/5. These approaches allowed us to identify cohesin subunits and CUX1 in proximity to IRX3 *in vitro* and *in vivo*, although we cannot state which proteins bind directly to IRX3. The lack of transcriptional change of cell cycle regulators in *Irx3/5* mutants combined with their physical association with regulators of sister chromatid segregation raises the possibility that IRX3/5 have nontranscriptional functions in addition to their transcriptional roles during pattern specification. Cohesin itself plays a dual role in segregating sister chromatids and marking gene enhancers throughout the cell cycle to facilitate transcriptional memory after cell division (Yan et al., 2013). Our data do not distinguish whether the binding of IRX proteins with cohesin regulators and with CUX1 occurs in a complex that regulates chromatid segregation directly or upon chromatin at developmentally active loci. Therefore a coincidental role for IRX3/5 in the transcriptional regulation of other signalling pathways, or potential participation of IRX3/5 in an indirect nontranscriptional process such as CUX1/2-mediated DNA damage

Development (2020) 17, dev180042. doi:10.1242/dev.180042

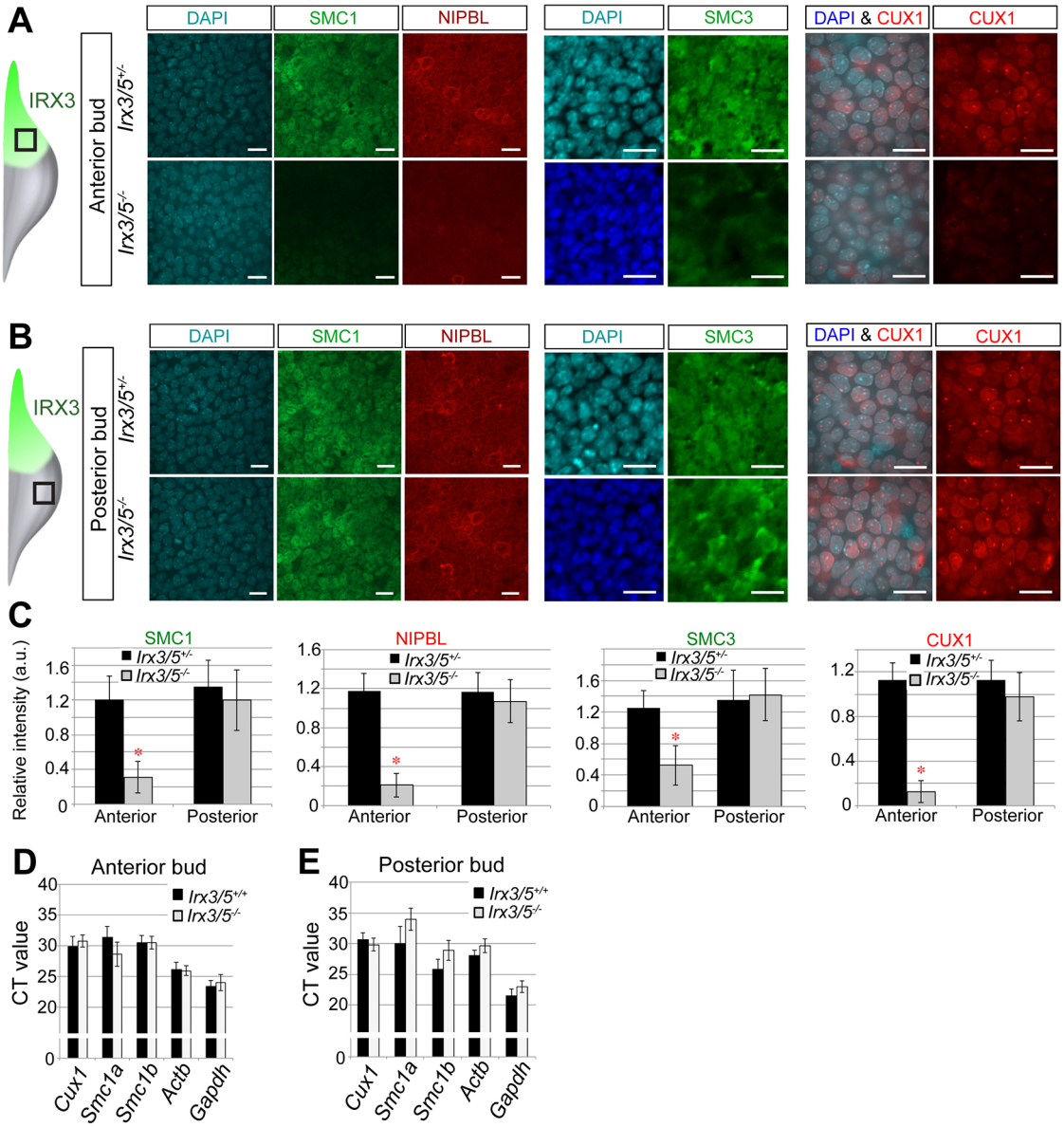

Fig. 5. IRX3/5 maintain cohesin subunits and CUX1 *in vivo*. (A,B) Immunofluorescence intensities of SMC1, NIPBL, SMC3 and CUX1 were diminished in the absence of *Irx3/5* in anterior (A), but not posterior (B), limb bud mesoderm. (C) Quantification of A and B (29-32 som.; *n*=3 embryos per condition; **P*=0.008 for anterior SMC1, **P*=0.003 for anterior NIPBL, **P*=0.004 for anterior SMC3, **P*=0.004 for anterior CUX1; unpaired, two-tailed *t*-test, error bars indicate s.e.m.). (D,E) Transcription of *Smc1a*, *Smc1b* and *Cux1* were unchanged by real time RT-PCR in anterior and posterior limb bud tissue in *Irx3/5*$^{+/-}$ and *Irx3/5*$^{-/-}$ embryos (29-30 som., *n*=3 embryos for each of three independent experiments). Error bars indicate s.e.m. Scale bars: 20 µm.

repair (Pal et al., 2015; Ramdzan et al., 2015, 2014; Iulianella et al., 2008) that regulates mitosis is possible. In principle, diminished cohesin may be associated with premature chromatid separation and/or chromatin bridges. Cohesin was originally identified as a regulator of sister chromatid cohesion, but it also organises interphase chromatin loops (Hadjur et al., 2009; Mishiro et al., 2009), spatial organisation of DNA (Guillou et al., 2010) and telomere replication (Remeseiro et al., 2012), making it somewhat challenging to predict the outcome of downregulation in different contexts. Genetic loss of cohesin has been shown to result in aneuploidy *in vivo* that corresponds to anaphase chromatin bridge formation *in vitro* (Remeseiro et al., 2012) and to lagging chromosomes in plant cells (He et al., 2019). The mutant phenotypes we observed may be the result of overlapping functions of cohesin and possibly of other regulators, such as condensin and CUX1. The mechanism by which multiple cohesin subunits are lost in the absence of *Irx3/5* is not clear, especially as only a small fraction of those proteins appear to be associated with IRX3/5 at any one time. One possibility is that IRX3/5 are intermittently required as accessory subunits which contribute to the formation or stabilisation of the cohesin complex. The Iro box is a poorly characterised IRX domain that may bind to unexpected partners (Barrios et al., 2015) to mediate such a function. IRX proteins may modify sister chromatid segregation and transcriptional activation as do other accessory subunits of cohesin such as BRCA2, PDS5, OCT4, and SALL4 modify (Abboud et al., 2015; Misulovin et al., 2018). Other potential mechanisms involve control over the translation of cell division-related transcripts, possibly in conjunction with cohesin itself (Xu et al., 2015), and the intriguing possibility that IRX3/5 function as pioneer transcription factors which make chromatin accessible for cohesin or CUX1 accumulation at

Development (2020) 17, dev180042. doi:10.1242/dev.180042

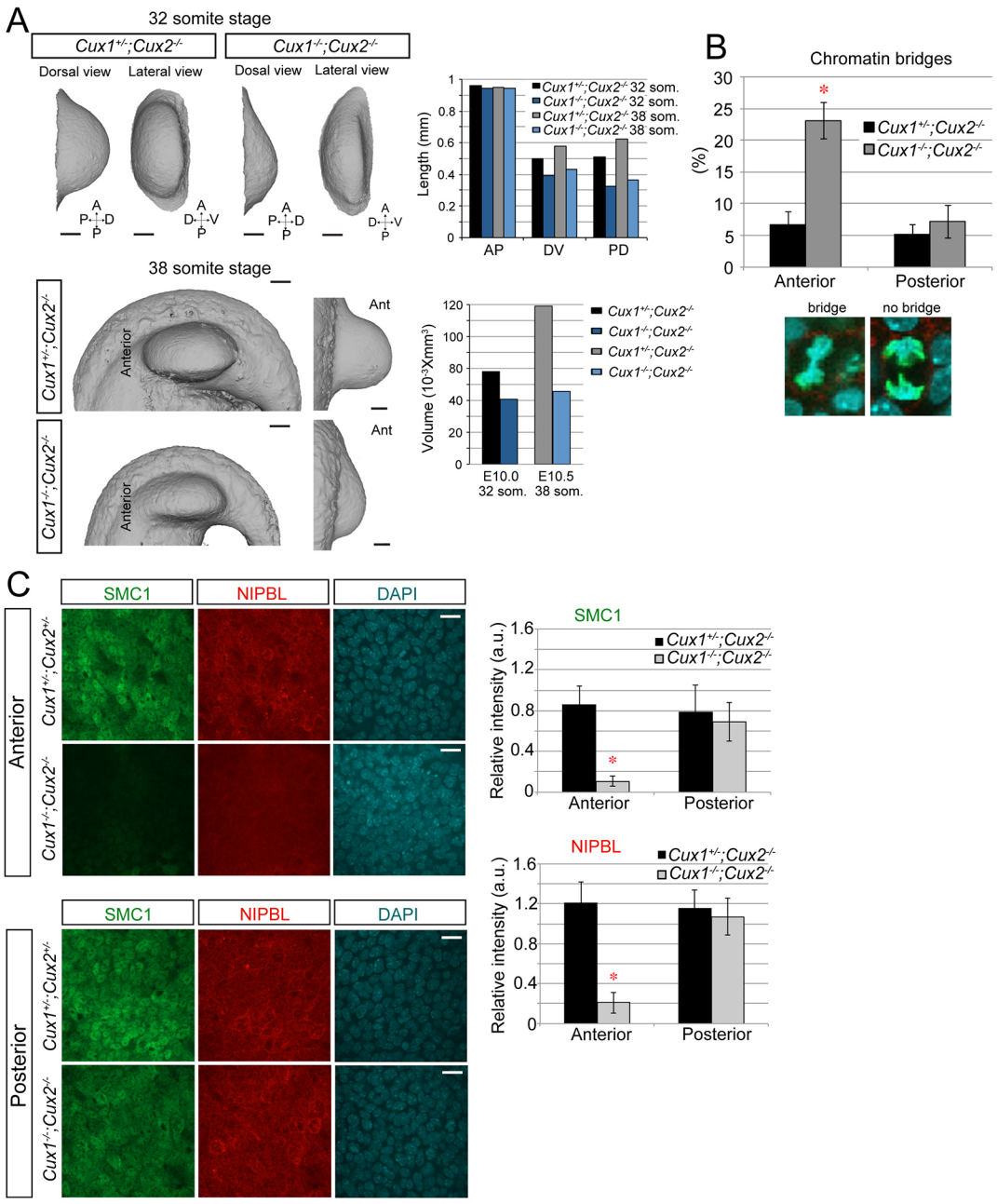

Fig. 6. *Cux1/2* share overlapping functions with *Irx3/5*. (A) *Cux1/2*$^{-/-}$ double mutant embryos at 32-38 som. have smaller hindlimb buds partly owing to PD undergrowth that is most pronounced in the anterior region by 38 som. (B) Static confocal imaging of anti-pHH3 immunostained embryos show chromatin bridges were relatively abundant among *Cux1/2*$^{-/-}$ mutant mesodermal cells in the anterior hindlimb field at 29-30 som. (**P*=0.018, unpaired, two-tailed *t*-test). (C) Section immunostaining revealed diminished anterior hindlimb SMC1 (*n*=3, **P*=0.002, unpaired, two-tailed *t*-test) and NIPBL (*n*=3, **P*=0.002, unpaired, two-tailed *t*-test) in 29-30 som. *Cux1/2*$^{-/-}$ mutants. AP, anteroposterior; DV, dorsoventral; PD, proximodistal. Error bars denote s.e.m. Scale bars: 200 µm (A); 20 µm (C).

transcriptionally active sites. Substantial further investigation is required to test these speculations. A somewhat puzzling observation in this study is that the fundamental process of mitotic chromatid segregation is regulated in a regional fashion. An upstream signalling or indirect mechanism may help to explain this observation, although other organ- and maturation-specific functions of cohesin and other fundamental cell division processes have been identified in *Drosophila* and mouse embryos (Song et al., 2017; Smith et al., 2014; Kim et al., 2019). Developmental complexity may have evolved in concert with the expression domains of Irx genes. Overall, evidence of interdependent protein expression and functional overlap shown by our mutant analyses suggests cooperation between these regulators, a concept that is supported by the occurrence of tibial deficiency in cohesinopathies (Pfeiffer and Correll, 1993) and in *Irx3/5* mutant mice (Li et al., 2014). Cell death, especially at later stages of limb bud development (Li et al., 2014), likely partially underlies undergrowth, dysmorphology and skeletal defects in *Irx3/5* mutants. However, the majority of cells that managed to separate despite a chromatin bridge exhibited disoriented planes of division and deficient intercalations that were associated with altered trajectories of mesodermal cells, suggesting those processes also contribute to the dysmorphology observed in mutants. Basal mechanisms of pattern formation, such as reaction-diffusion (Raspopovic et al., 2014) and morphogen gradients (Woolley et al., 2014), invoke distinct modes of

Development (2020) 17, dev180042. doi:10.1242/dev.180042

molecular interaction but are each affected by the volume and shape of the tissue in which they function (Dekanty and Milán, 2011). It is therefore conceivable that IRX3/5 influence skeletal pattern by coordinating the form of the early hindlimb bud with the expression of patterning molecules such as GLI3 (Li et al., 2014). In *Drosophila*, the Iroquois protein Caupolican was also shown to regulate the size of developmental fields by binding to Cyclin-E-containing complexes (Barrios et al., 2015). Therefore, a dual transcriptional/nontranscriptional role for Iroquois is potentially conserved and may be common to other transcription factors in order to coordinate early tissue morphogenesis with subsequent pattern formation.

MATERIALS AND METHODS

Mouse strains

Analysis was performed using the following mouse strains: *Irx3/5*$^{+/-}$ (Li et al., 2014) [*Irx3* and *Irx5* were targeted separately in embryonic stem cells without affecting the intervening region as described previously (Li et al., 2014)], *Irx3-myc*, CAG::*H2B-GFP* [Jackson Laboratory, B6.Cg-Tg(HIST1H2BB/EGFP) 1 Pa/J; Hadjantonakis and Papaioannou, 2004], Confetti (Snippert et al., 2010), Esr1:Cre [Jackson Laboratory, B6N.129S6(Cg)-Esr1$^{tm1.1(cre)And/J}$; Lee et al., 2014], *Cux*$^{+/-}$ (Luong et al., 2002) and *Cux2*$^{+/-}$ (Iulianella et al., 2008). To generate conditional mutant embryos, flox/flox females carrying the appropriate fluorescent reporter were bred to flox/+;Cre males. All animal experiments were performed in accordance with protocols approved by the Hospital for Sick Children Animal Care Committee and the Canadian Council on Animal Care.

Optical projection tomography and limb bud morphology analysis

E9.5 mouse embryos were harvested and fixed in 4% paraformaldehyde overnight at 4°C. The OPT system was custom-built and has been fully described previously (Wong et al., 2013). The 3D datasets were reconstructed from auto-fluorescence projection images acquired over a 10 min scan time at an isotropic voxel size of 3.85 µm. The 3D surface renderings of the OPT data were generated by Amira software, version 5.3.3 (Visualization Sciences Group).

Live imaging and cell tracking

Three-dimensional time-lapse microscopy was performed on a Zeiss Lightsheet Z.1. microscope. Embryos were suspended in a solution of DMEM without phenol red containing 12.5% rat serum and 1% low-melt agarose (Invitrogen) in a glass capillary tube. Once the agarose had solidified, the capillary was submerged into an imaging chamber containing DMEM without phenol red, and the agarose plug was partially extruded from the capillary until the portion containing the embryo was completely outside of the capillary. The temperature of the imaging chamber was maintained at 37°C with 5% CO_2. Images were acquired using a 20×/1.0 objective with dual-side illumination, and a *z*-interval of 0.479 µm. All experiments were imaged in multi-view mode with three evenly spaced views spanning ∼90° (from a frontal view to a sagittal view of the mandibular arch). Images were acquired for 3-4 h with 10 min intervals. Fluorescent beads (Fluospheres 1 µm, Thermo Fisher Scientific, 1:10^6) were used as fiducial markers for 3D reconstruction and to aid in drift-correction for cell tracking. Multi-view processing was performed using Zen 2014 SP1 software to merge the three separate views and generate a single 3D image. Further analysis and cell tracking were performed using Arivis Vision4D software.

To correct for drift, the frame-by-frame displacement of red fluorescent beads that were embedded adjacent to the embryo within the agarose plug used in the light sheet microscope was calculated. These displacements were imported into MATLAB for initial track concatenation and drift correction. Track and segment information and validity were acquired on Arivis. The concatenation function returned drift corrected tracks that were filtered to only include valid tracks. Tracks could then be plotted, and end-to-end displacements calculated and plotted.

Confocal live imaging was performed as described previously (Wyngaarden et al., 2010; Lau et al., 2015). Briefly, embryos were submerged in 50% rat serum in DMEM (Invitrogen) in a 25 mm imaging chamber. Cheese cloth was used to immobilise the embryo and position the initiating limb bud directly against the cover glass. Embryos were imaged in a humidified chamber at 37°C in 5% CO_2. Time lapse images were acquired on a Zeiss LSM510 META confocal microscope at 20× or 40× magnification or on a Quorum spinning disk confocal microscope at 20× magnification. Images were processed using Volocity software or ImageJ.

Daughter cell intercalations in the anterior hindlimb fields of E9.75 Esr1:Cre;Confetti embryos were identified manually. A 20× objective was used to visualise ∼150 cells through 20 frames at 5 min intervals. Statistical comparisons of WT and mutant conditions were performed using the Student's *t*-test.

For long-term cell displacement analysis, E9.75 Esr1:Cre;Confetti embryos were collected 24 h after intraperitoneal injection of pregnant females with tamoxifen (doses given in Fig. S1) and placed in a 25 mm imaging chamber coated with 2% agarose containing 5% fetal bovine serum (FBS) in DMEM. Embryos were immobilised using pulled glass needles to pin the head and tail to the agarose. Images were acquired using a Quorum spinning-disk confocal microscope at 20× magnification to encompass the entire hindlimb field, and were stitched together using ImageJ. A reference point was arbitrarily chosen near the centre of the field for later comparison. Embryos were then incubated in roller culture in 50% rat serum in DMEM for 8 h before reimaging as before.

DNA content analysis *in vivo*

E10.5 limb buds were dissected from embryos in ice-cold PBS and then treated with trypsin at 37°C to dissociate limb bud cells. PBS with 2% FBS was used to resuspend cell pellets after centrifugation. Filtered cells were then fixed with ice-cold 80% EtOH overnight at 4°C. After removal of EtOH, fixed cells were washed, resuspended and stained with DAPI solution (Sigma-Aldrich) for 30 min in darkness. Stained cells were analysed on a FACSCanto II (Becton-Dickinson) and data acquired using CellQuest (BD Biosciences). Data were analysed with FlowJo (Tree Star) using the cell cycle platform.

Double-pulse analysis for cell cycle time estimation *in vivo*

Pregnant females were injected first with CldU intraperitoneally at E9.75 and then with IddU after 2.5 h. After 30 min (following the second injection) embryos were dissected in cold PBS and fixed with 4% paraformaldehyde overnight at 4°C. Whole-mount immunofluorescence of CldU and IddU was performed. Cell cycle time was measured by assessing the proportion of cells that exited S phase between the two injections (Boehm et al., 2010; Tao et al., 2019).

RNA-seq

Tissues posterior to the 20th somite level were collected from 25/26 som. mouse embryos, and total RNA was isolated using the RNeasy micro kit (QIAGEN) according to the manufacturer's instructions. Then, 500 ng of RNA from each embryo was subjected to library synthesis with the TruSeq RNA v2 reagents. The library was size-selected to produce insert sizes of ∼200 bp, and a 50 bp pair-end run was performed for >20 million reads for each library. The raw RNA-seq reads were mapped to the mouse genome (mm10) using TopHat (v2.0.13) and Cufflinks (v2.2.1) pipeline. Differential expression analysis was performed by edgeR (Robinson et al., 2010); Fisher's exact test was used to determine significance. NCBI BioSample accession numbers for the full dataset are in Table S2.

Proximity biotinylation coupled to mass spectrometry

Constructs for BioID experiments were generated via Gateway cloning into pDEST 5′ BirA*-FLAG-pcDNA5-FRT-TO (Lambert et al., 2015). Entry clones for Irx3 and Irx5 were first generated by performing PCR reaction from plasmids with full length cDNA (Flag-Irx3 in pENTR2B and Flag-Irx5 in pENTR2B). Primers for Irx3 were ggggacaactttgtacaaaaaagttggcaccAT-GTCCTTCCCCCAGCTCG and ggggacaactttgtacaagaaagttgggtaTTAAGA-CGAGGAGAGAGCTGATAAG. Primers for Irx5 were ggggacaacttt-gtacaaaaaagttggcaccATGTCCTACCCGCAGGGCT and

Development (2020) 17, dev180042. doi:10.1242/dev.180042

ggggacaactttgtacaagaaagttgggtaTTAAATGTCGGACATACCTTTCTTCA-AC. Lower case bases refer to sequences used for the Gateway BP clonase reaction, while the upper case bases have homology with Irx3/5 genes.

HEK293 cell pellets harvested from two 15 cm plates were thawed in 1.5 ml ice cold RIPA buffer containing 50 mM Tris-HCl (pH 7.5), 150 mM NaCl, 1% NP-40, 1 mM EDTA, 1 mM EGTA, 0.1% SDS and 0.5% sodium deoxycholate. PMSF (1 mM), DTT (1 mM) and Sigma protease inhibitor cocktail (P8340, Sigma-Aldrich, 1:500) were added immediately before use. The samples were sonicated at 4°C using three 10 s bursts with 2 s pauses at 35% amplitude. Then, 100 units of benzonase was added and the lysates were incubated at 4°C for an hour with rotation. For each sample, 60 µl of streptavidin-sepharose bead slurry (17-5113-01, GE Healthcare) were pre-washed three times with 1 ml of lysis buffer by pelleting the beads with gentle centrifugation (∼500 ***g***) and aspirating off the supernatant before adding the next wash. Biotinylated proteins were captured on pre-washed streptavidin beads for 3 h at 4°C with rotation. The beads were then gently pelleted and the unbound supernatant was saved for further analysis. The beads were then washed twice with 1 ml RIPA buffer and three times with 1 ml 50 mM ammonium bicarbonate (pH 8.0). Following the final wash, the beads were pelleted and any excess liquid was aspirated off. Beads were then resuspended in 100 µl of 50 mM ammonium bicarbonate, and 1 µg of trypsin solution was added. The samples were incubated overnight at 37°C with rotation and then an additional 1 µg of trypsin was added, followed by a further incubation for 2-4 h. The beads were pelleted and the supernatant was transferred to a fresh tube. The beads were rinsed twice with 100 µl HPLC grade water and the wash fraction was combined with the supernatant. The peptide solution was acidified with 50% formic acid to a final concentration of 2% and the samples were placed in a speedvac to dry. Tryptic peptides were resuspended in 25 µl 5% formic acid and stored at −80°C until analysed by mass spectrometry.

Mass spectrometry analysis

BioID samples and controls were analysed by mass spectrometry (MS) in two biological replicates. We loaded 5 µl of each sample at 400 nl/min onto a 75 µm×12 cm emitter packed with 3 µm ReproSil-Pur C_{18}-AQ (Dr Maisch HPLC GmbH). The peptides were eluted from the column over a 90 min gradient generated by a NanoLC-Ultra 1D plus (Eksigent) nano-pump and analysed on a LTQ Orbitrap Velos instrument (Thermo Electron). The gradient was delivered at 200 nl/min starting from 2% acetonitrile with 0.1% formic acid to 35% acetonitrile with 0.1% formic acid over 90 min followed by a 15 min clean-up at 80% acetonitrile with 0.1% formic acid, and a 15 min equilibration period back to 2% acetonitrile with 0.1% formic acid for a total of 120 min. To minimise carryover between each sample, the analytical column was washed for 3 h by running an alternating sawtooth gradient from 35% acetonitrile with 0.1% formic acid to 80% acetonitrile with 0.1% formic acid, holding each gradient concentration for 5 min. Analytical column and instrument performance were verified after each sample by loading 30 fmol bovine serum albumin (BSA) tryptic peptide standard (Michrom Bioresources Inc.) with 60 fmol α-Casein tryptic digest and running a short 30 min gradient. The LTQ Orbitrap Velos was operated with Xcalibur 2.0 in data-dependent acquisition mode with the following parameters: one centroid MS (mass range, 400 to 2000) followed by MS-MS on the 10 most abundant ions. General parameters were as follows: activation type=CID, isolation width=1 mass/charge ratio (m/z), normalised collision energy=35, activation Q=0.25, activation time=10 ms. For data-dependent acquisition, the minimum threshold was 500, the repeat count=1, repeat duration=30 s, exclusion size list=500, exclusion duration=30 s and exclusion mass width (by mass)=low 0.6, high 1.2.

MS data analysis

Two biological replicates of each bait were analysed by BioID-MS against a series of controls which included BirA alone, BirA fused to GFP, and cells expressing different nuclear proteins (KATs, BRPF3, BRD4, CBX3). Mass spectrometry data generated using a LTQ Orbitrap Velos were stored, searched and analysed using the ProHits laboratory information management system (LIMS) platform (Liu et al., 2010). Within ProHits, the resulting RAW files were converted to mzXML using ProteoWizard (v3.0.4468) and then searched using Mascot (v2.3.02). The spectra were searched with the RefSeq database (version 53, May 23th, 2013) acquired from NCBI against a total of 34,374 human and adenovirus sequences supplemented with 'common contaminants' from the Max Planck Institute (http://lotus1.gwdg.de/mpg/mmbc/maxquant_input.nsf/7994124a4298328fc125748d0048fee2/$FILE/contaminants.fasta) and the Global Proteome Machine (GPM; http://www.thegpm.org/crap/index.html). The database parameters were set to search for tryptic cleavages, allowing up to two missed cleavage sites per peptide with a mass tolerance of 50 ppm for precursors with charges of 2+ to 4+ and a tolerance of +/−0.6 amu for fragment ions. Variable modifications were selected for deamidated asparagine and glutamine and oxidised methionine. Significance analysis of interactome (SAINT) express version 3.3 (Teo et al., 2014) was used as a statistical tool to calculate the probability value of each potential protein-protein interaction from background contaminants using default parameters. Dot plots of Irx3 and Irx5 interactomes obtained by BioID were generated using custom built proteomics data visualisation tools (Knight et al., 2015). All MS files used in this study were deposited at Proteome Exchange (http://proteomecentral.proteomexchange.org/cgi/GetDataset?ID=PXD004309).

Immunofluorescence

E9.5-10.5 mouse embryos were fixed overnight in 4% paraformaldehyde in PBS followed by three washes in PBS. Embryos were permeabilised in 0.1% Triton X-100 in PBS for 20 min and blocked in 5% normal donkey serum (in 0.05% Triton X-100 in PBS) for 1 h. Embryos were incubated in primary antibody for 5 h at room temperature, followed by overnight incubation at 4°C. Embryos were washed in 0.05% Triton X-100 in PBS (four washes, 20 min each), and then incubated in secondary antibody for 3-5 h at room temperature. Embryos were washed (four washes, 20 min each), followed by a final wash overnight at 4°C, and stored in PBS. Images were acquired using a Quorum spinning disk confocal microscope and Nikon A1 confocal microscope at 10×, 20×, or 40× magnification or Leica TCS SP8 STED 3× microscopy at 100× magnification, and image analysis was performed using Volocity software and ImageJ. Relative fluorescence intensity was derived by normalising intensity of immunostaining to the corresponding DAPI stain intensity (set at 1) within a field of 15 mesodermal cells and averaged over three embryos, similar to a procedure we described previously (Lau et al., 2015).

Antibodies company and catalogue number

IRX3 [Novus Biologicals, 1D7, H0079191-M05, mouse, 1:250 – used for immunofluorescence (IF)]; IRX3 (Santa Cruz Biotechnology, G-6, 166877, mouse, 1:100 – used for co-IP *in vivo*); SMC1 (Abcam, ab21583, rabbit, 1:250 IF, 1:1000 – used for immunoblotting (IB); SMC3 (Novus Biological, NB100-207 IF, *in vitro* IB; Abcam, ab9263, 1:1000 *in vivo* IB); NIPBL (Santa Cruz Biotechnology, C-9, sc-374625, 1:1000); CUX1 (Abcam, ab140042, mouse, 1:250 IF, *in vitro* IB; Abcam, ab230844, rabbit, 1:2500 *in vivo* IB); IgG (NA931V, GE Healthcare, 1:100) or donkey anti-rabbit IgG (NA934V, GE Healthcare, 1:100) co-IP *in vitro*, IgG (Santa Cruz Biotechnology, 2343, 1:100) co-IP *in vivo*; Caspase-3 (BD Biosciences, 559565, 1:250); F-Actin (Alexa Fluor 633 Phalloidin, Thermo Fisher Scientific, A22284, 1:1000).

Co-immunoprecipitation

In vitro

HEK293T cells were transfected with full-length FLAG-Irx3 that was cloned into the pDNR-CMV expression construct (Zhang et al., 2011) (Clontech) using Lipofectamine 2000 (11668027, Life Technologies). Cell lysates were prepared after 2 days and co-IP assays were performed using Protein G PLUS-Agarose (sc-2002, Santa Cruz Biotechnology) and anti-Irx3 antibody (homemade). Proteins were resolved by SDS-PAGE, transferred to PVDF membrane (IPVH00010, Millipore) and detected by HRP sheep anti-mouse IgG (NA931V, GE Healthcare, 1:100) or donkey anti-rabbit IgG (NA934V, GE Healthcare, 1:100) and a chemiluminescence system. Input lanes represent immunoprecipitated lysate that was run on separate gels without western blot antibody or further treatment.

Development (2020) 17, dev180042. doi:10.1242/dev.180042

In vivo

We lysed 30 E10.5 hindlimb buds in PLC lysis buffer [50 mM HEPES (pH 7.5), 150 mM NaCl, 1.5 mM $MgCl_2$, 1 mM EGTA, 10% glycerol, 1% TritonX-100, protease inhibitors (11836153001, Roche)] using the Precellys Lysing kit (KT03961-1-003.2) using 200-250 µg cell lysate per sample. Then 50% protein A/G-agarose was prepared with cold PBS, and 50% A/G-agarose working fluid was added to the sample (100 mM/ml). The concentration of total sample protein was determined by bicinchoninic acid (BCA) at 4°C for 10 min. Cell lysates were prepared after 2 days and co-IP assays were performed by using Protein G PLUS-Agarose (sc-2002, Santa Cruz Biotechnology) and anti-IRX3 (Santa Cruz Biotechnology) or anti-IgG antibody.

Western blotting

In vitro

HEK293 cell were lysed in PLC lysis buffer [50 mM HEPES (pH 7.5), 150 mM NaCl, 1.5 mM $MgCl_2$, 1 mM EGTA, 10% glycerol, 1% TritonX-100, protease inhibitors (11836153001, Roche)]. Proteins were separated by SDS-PAGE, transferred to PVDF membranes (PerkinElmer), and incubated with primary antibodies overnight at 4°C. Immunoblots were developed using HRP-conjugated secondary antibodies and Western lighting Plus-ECL (NEL104001EA, PerkinElmer).

In vivo

Proteins were resolved by SDS-PAGE, transferred to PVDF membrane (IPVH00010, Millipore) and detected by HRP sheep anti-mouse IgG (NA931V, GE Healthcare, 1:100) or donkey anti-rabbit IgG (NA934V, GE Healthcare, 1:100), and a chemi-luminescence system. The membranes were cleaned three times with Tris buffered saline with Tween (TBST) solution for 10 min each time. The skimmed milk was sealed, and 3 ml added to the antibody incubator. The membranes were sealed for 1 h at room temperature. Membranes were cleaned with TBST solution three times, for 10 min each time; incubation with the primary antibody – anti-SMC1 antibody (ab21583, Abcam, rabbit, 1:1000), anti-SCM3 antibody (ab9263, Abcam, rabbit, 1:1000), anti-CUX1 antibody (ab230844, Abcam, rabbit, 1:2500) or anti-IgG (Santa Cruz Biotechnology, 2343, 1:100) – was carried out overnight at 4°C. Incubation with the second antibody was at room temperature for 1 h. Finally, an appropriate amount of luminescent solution (A and B liquid volumes were mixed) was used to incubate the membrane for 3 min; the gel imaging system was exposed and Quantity-One software was used to analyse the protein content.

Quantitative real-time PCR

RNA was isolated from E10.5 hindlimbs. At least three independent biological replicates were used, and each experiment was repeated at least twice. Reactions utilised TaqMan Universal PCR master mix (Applied Biosystems), and TaqMan Gene Expression Assay probes for mouse *Cux1* (Forward, CGGGGGAACAGGTTTCCAAT; Reverse, GCATTAGCTGT-CGCTGGAGA), *Smc1a* (Forward, ATTGGACCCAATGGCTCTGG; Reverse, CTCCATGTATCAGGTCCCGC), *Smc1b* (Forward, GGTCAT-CGGCCCTTTCAAGA; Reverse, CAGGTTTTCCAGTATGTGCTCC), *beta-actin* (PrimerBank ID 6671509a1), *Gapdh* (Mm03302249_g1) was used as the endogenous control for target gene normalisation. Gene expressions were analysed using the 2DDCt method (Livak et al., 2013). Statistical significance was determined using Student's *t*-test. Error bars denote s.d.

In situ proximity ligation assay (PLA)

PLA (DUO92101, Sigma-Aldrich) was performed in a similar manner as standard immunohistochemistry until the secondary antibody incubation step. PLA probe dilution/incubation time, rolling circle amplification times and polymerase concentrations were optimised for frozen tissue sections. For detection of IRX3 in close proximity to either SMC1 or CUX1, two primary antibodies raised in different species were used. Secondary anti-mouse (PLUS) and anti-rabbit (MINUS) antibodies conjugated to complementary oligonucleotides provided in the kit were used. Slides were incubated overnight at 4°C for primary antibody reaction and then 2 h at 37°C in blocking solution containing PLUS and MINUS probes. A polymerase dilution of 1/80 was optimal for single recognition; incubation time was 2 h under gentle agitation.

Acknowledgements

We thank Drs Jacques Drouin, Cliff Tabin, Rodrigo Fernandez-Gonzalez and Tae-Hee Kim for critical comments on the manuscript.

Competing interests

The authors declare no competing or financial interests.

Author contributions

Conceptualization: H.T., C.-c.H., S.H.; Methodology: H.T., J.-P.L., N.A.H., Y.K., M.Z., A.-C.G., C.-c.H., S.H.; Formal analysis: H.T., J.-P.L., Y.K., A.-C.G., C.-c.H., S.H.; Investigation: H.T., J.-P.L., T.M.Y., M.Z., N.A.H., D.L., K.L., K.S., V.P., X.Z., W.G., X.X.C., G.A., D.J.G., A.I.; Resources: D.J.G., R.M.H., Y.S., A.I., Y.K., A.-C.G., C.-c.H., S.H.; Writing - original draft: S.H.; Writing - review & editing: C.-c.H., S.H.; Visualization: H.T., J.-P.L., T.M.Y., M.Z., W.G., G.A.; Supervision: R.M.H., Y.K., A.-C.G., C.-c.H., S.H.; Funding acquisition: C.-c.H., S.H.

Funding

This work was supported by the Canadian Institutes of Health Research (137092 to S.H. and C.-c.H.) and by the National Institute of Arthritis and Musculoskeletal and Skin Diseases of the National Institutes of Health (R01AR064195 to Y.K.). Deposited in PMC for release after 12 months.

Data availability

All mass spectrometry files used in this study were deposited at MassIVE (http://massive.ucsd.edu) under accession number MSV000079812 as well as to the ProteomeXchange (PXD004309). NCBI BioSample accession numbers for the full RNA-seq datasets generated in this study are in Table S2.

Supplementary information

Supplementary information available online at
https://dev.biologists.org/lookup/doi/10.1242/dev.180042.supplemental

References

Abboud, N., Morris, T. M., Hiriart, E., Yang, H., Bezerra, H., Gualazzi, M.-G., Stefanovic, S., Guénantin, A.-C., Evans, S. M. and Pucéat, M. (2015). A cohesin-OCT4 complex mediates Sox enhancers to prime an early embryonic lineage. *Nat. Commun.* **6**, 6749. doi:10.1038/ncomms7749

Barrios, N., González-Pérez, E., Hernández, R. and Campuzano, S. (2015). The homeodomain iroquois proteins control cell cycle progression and regulate the size of developmental fields. *PLoS Genet.* **11**, e1005463. doi:10.1371/journal.pgen.1005463

Bilioni, A., Craig, G., Hill, C. and Mcneill, H. (2005). Iroquois transcription factors recognize a unique motif to mediate transcriptional repression in vivo. *Proc. Natl. Acad. Sci. USA* **102**, 14671-14676. doi:10.1073/pnas.0502480102

Boehm, B., Westerberg, H., Lesnicar-Pucko, G., Raja, S., Rautschka, M., Cotterell, J., Swoger, J. and Sharpe, J. (2010). The role of spatially controlled cell proliferation in limb bud morphogenesis. *PLoS Biol.* **8**, e1000420. doi:10.1371/journal.pbio.1000420

Burglin, T. R. (1997). Analysis of TALE superclass homeobox genes (MEIS, PBC, KNOX, Iroquois, TGIF) reveals a novel domain conserved between plants and animals. *Nucleic Acids Res.* **25**, 4173-4180. doi:10.1093/nar/25.21.4173

Capdevila, J., Tsukui, T., Rodriquez Esteban, C., Zappavigna, V. and Izpisua Belmonte, J. C. (1999). Control of vertebrate limb outgrowth by the proximal factor Meis2 and distal antagonism of BMPs by Gremlin. *Mol. Cell* **4**, 839-849. doi:10.1016/S1097-2765(00)80393-7

Cavodeassi, F., Modolell, J. and Gomez-Skarmeta, J. L. (2001). The Iroquois family of genes: from body building to neural patterning. *Development* **128**, 2847-2855.

Cheng, C. W., Chow, R. L., Lebel, M., Sakuma, R., Cheung, H. O.-L., Thanabalasingham, V., Zhang, X., Bruneau, B. G., Birch, D. G., Hui, C.-C. et al. (2005). The Iroquois homeobox gene, Irx5, is required for retinal cone bipolar cell development. *Dev. Biol.* **287**, 48-60. doi:10.1016/j.ydbio.2005.08.029

Costantini, D. L., Arruda, E. P., Agarwal, P., Kim, K.-H., Zhu, Y., Zhu, W., Lebel, M., Cheng, C. W., Park, C. Y., Pierce, S. A. et al. (2005). The homeodomain transcription factor Irx5 establishes the mouse cardiac ventricular repolarization gradient. *Cell* **123**, 347-358. doi:10.1016/j.cell.2005.08.004

Dekanty, A. and Milán, M. (2011). The interplay between morphogens and tissue growth. *EMBO Rep.* **12**, 1003-1010. doi:10.1038/embor.2011.172

Demare, L. E., Leng, J., Cotney, J., Reilly, S. K., Yin, J., Sarro, R. and Noonan, J. P. (2013). The genomic landscape of cohesin-associated chromatin interactions. *Genome Res.* **23**, 1224-1234. doi:10.1101/gr.156570.113

Fornasiero, E. F. and Opazo, F. (2015). Super-resolution imaging for cell biologists: concepts, applications, current challenges and developments. *Bioessays* **37**, 436-451. doi:10.1002/bies.201400170

Gaborit, N., Sakuma, R., Wylie, J. N., Kim, K.-H., Zhang, S.-S., Hui, C.-C. and Bruneau, B. G. (2012). Cooperative and antagonistic roles for Irx3 and Irx5 in cardiac morphogenesis and postnatal physiology. *Development* **139**, 4007-4019. doi:10.1242/dev.081703

Gómez-Skarmeta, J. L. and Modolell, J. (2002). Iroquois genes: genomic organization and function in vertebrate neural development. *Curr. Opin. Genet. Dev.* **12**, 403-408. doi:10.1016/S0959-437X(02)00317-9

Gros, J., Hu, J. K.-H., Vinegoni, C., Feruglio, P. F., Weissleder, R. and Tabin, C. J. (2010). WNT5A/JNK and FGF/MAPK pathways regulate the cellular events shaping the vertebrate limb bud. *Curr. Biol.* **20**, 1993-2002. doi:10.1016/j.cub.2010.09.063

Guillou, E., Ibarra, A., Coulon, V., Casado-Vela, J., Rico, D., Casal, I., Schwob, E., Losada, A. and Mendez, J. (2010). Cohesin organizes chromatin loops at DNA replication factories. *Genes Dev.* **24**, 2812-2822. doi:10.1101/gad.608210

Hadjantonakis, A.-K. and Papaioannou, V. E. (2004). Dynamic in vivo imaging and cell tracking using a histone fluorescent protein fusion in mice. *BMC Biotechnol.* **4**, 33. doi:10.1186/1472-6750-4-33

Hadjur, S., Williams, L. M., Ryan, N. K., Cobb, B. S., Sexton, T., Fraser, P., Fisher, A. G. and Merkenschlager, M. (2009). Cohesins form chromosomal cis-interactions at the developmentally regulated IFNG locus. *Nature* **460**, 410-413. doi:10.1038/nature08079

He, Y., Wang, J., Qi, W. and Song, R. (2019). Maize Dek15 encodes the cohesin-loading complex subunit SCC4 and is essential for chromosome segregation and kernel development. *Plant Cell* **31**, 465-485. doi:10.1105/tpc.18.00921

Hirano, T. (2006). At the heart of the chromosome: SMC proteins in action. *Nat. Rev. Mol. Cell Biol.* **7**, 311-322. doi:10.1038/nrm1909

Iulianella, A., Vanden Heuvel, G. and Trainor, P. (2003). Dynamic expression of murine Cux2 in craniofacial, limb, urogenital and neuronal primordia. *Gene Expr. Patterns* **3**, 571-577. doi:10.1016/S1567-133X(03)00123-6

Iulianella, A., Sharma, M., Durnin, M., Vanden Heuvel, G. B. and Trainor, P. A. (2008). Cux2 (Cutl2) integrates neural progenitor development with cell-cycle progression during spinal cord neurogenesis. *Development* **135**, 729-741. doi:10.1242/dev.013276

Jeppsson, K., Kanno, T., Shirahige, K. and Sjögren, C. (2014). The maintenance of chromosome structure: positioning and functioning of SMC complexes. *Nat. Rev. Mol. Cell Biol.* **15**, 601-614. doi:10.1038/nrm3857

Kakui, Y. and Uhlmann, F. (2018). SMC complexes orchestrate the mitotic chromatin interaction landscape. *Curr. Genet.* **64**, 335-339. doi:10.1007/s00294-017-0755-y

Kawakami, Y., Uchiyama, Y., Rodriguez Esteban, C., Inenaga, T., Koyano-Nakagawa, N., Kawakami, H., Marti, M., Kmita, M., Monaghan-Nichols, P., Nishinakamura, R. et al. (2009). Sall genes regulate region-specific morphogenesis in the mouse limb by modulating Hox activities. *Development* **136**, 585-594. doi:10.1242/dev.027748

Kawauchi, S., Calof, A. L., Santos, R., Lopez-Burks, M. E., Young, C. M., Hoang, M. P., Chua, A., Lao, T., Lechner, M. S., Daniel, J. A. et al. (2009). Multiple organ system defects and transcriptional dysregulation in the Nipbl(+/−) mouse, a model of Cornelia de Lange syndrome. *PLoS Genet.* **5**, e1000650. doi:10.1371/journal.pgen.1000650

Ke, R., Nong, R. Y., Fredriksson, S., Landegren, U. and Nilsson, M. (2013). Improving precision of proximity ligation assay by amplified single molecule detection. *PLoS ONE* **8**, e69813. doi:10.1371/journal.pone.0069813

Kim, N. and Song, K. (2013). KIFC1 is essential for bipolar spindle formation and genomic stability in the primary human fibroblast IMR-90 cell. *Cell Struct. Funct.* **38**, 21-30. doi:10.1247/csf.12014

Kim, K.-H., Rosen, A., Bruneau, B. G., Hui, C.-C. and Backx, P. H. (2012). Iroquois homeodomain transcription factors in heart development and function. *Circ. Res.* **110**, 1513-1524. doi:10.1161/CIRCRESAHA.112.265041

Kim, D. I., Birendra, K. C., Zhu, W., Motamedchaboki, K., Doye, V. and Roux, K. J. (2014). Probing nuclear pore complex architecture with proximity-dependent biotinylation. *Proc. Natl. Acad. Sci. USA* **111**, E2453-E2461. doi:10.1073/pnas.1406459111

Kim, L.-H., Hong, S.-T. and Choi, K.-W. (2019). Protein phosphatase 2A interacts with Verthandi/Rad21 to regulate mitosis and organ development in Drosophila. *Sci. Rep.* **9**, 7624. doi:10.1038/s41598-019-44027-3

Knight, J. D. R., Liu, G., Zhang, J. P., Pasculescu, A., Choi, H. and Gingras, A.-C. (2015). A web-tool for visualizing quantitative protein-protein interaction data. *Proteomics* **15**, 1432-1436. doi:10.1002/pmic.201400429

Kschonsak, M. and Haering, C. H. (2015). Shaping mitotic chromosomes: from classical concepts to molecular mechanisms. *Bioessays* **37**, 755-766. doi:10.1002/bies.201500020

Lambert, J.-P., Tucholska, M., Go, C., Knight, J. D. R. and Gingras, A.-C. (2015). Proximity biotinylation and affinity purification are complementary approaches for the interactome mapping of chromatin-associated protein complexes. *J. Proteomics* **118**, 81-94. doi:10.1016/j.jprot.2014.09.011

Lau, K., Tao, H., Liu, H., Wen, J., Sturgeon, K., Sorfazlian, N., Lazic, S., Burrows, J. T. A., Wong, M. D., Li, D. et al. (2015). Anisotropic stress orients remodelling of mammalian limb bud ectoderm. *Nat. Cell Biol.* **17**, 569-579. doi:10.1038/ncb3156

Lee, S.-K., Jurata, L. W., Funahashi, J., Ruiz, E. C. and Pfaff, S. L. (2004). Analysis of embryonic motoneuron gene regulation: derepression of general activators function in concert with enhancer factors. *Development* **131**, 3295-3306. doi:10.1242/dev.01179

Lee, H., Kim, D.-W., Remedios, R., Anthony, T. E., Chang, A., Madisen, L., Zeng, H. and Anderson, D. J. (2014). Scalable control of mounting and attack by Esr1+ neurons in the ventromedial hypothalamus. *Nature* **509**, 627-632. doi:10.1038/nature13169

Li, D., Sakuma, R., Vakili, N. A., Mo, R., Puviindran, V., Deimling, S., Zhang, X., Hopyan, S. and Hui, C.-C. (2014). Formation of proximal and anterior limb skeleton requires early function of Irx3 and Irx5 and is negatively regulated by Shh signaling. *Dev. Cell* **29**, 233-240. doi:10.1016/j.devcel.2014.03.001

Liu, Y. and Robinson, D. (2018). Recent advances in cytokinesis: understanding the molecular underpinnings. *F1000Res* **7**, F1000 Faculty Rev-1849. doi:10.12688/f1000research.16502.1

Liu, G., Zhang, J., Larsen, B., Stark, C., Breitkreutz, A., Lin, Z.-Y., Breitkreutz, B.-J., Ding, Y., Colwill, K., Pasculescu, A. et al. (2010). ProHits: integrated software for mass spectrometry-based interaction proteomics. *Nat. Biotechnol.* **28**, 1015-1017. doi:10.1038/nbt1010-1015

Liu, W., Biton, E., Pathania, A., Matityahu, A., Irudayaraj, J. and Onn, I. (2019). Monomeric cohesin state revealed by live-cell single-molecule spectroscopy. *EMBO Rep.* **21**, e48211. doi:10.15252/embr.201948211

Livak, K. J., Wills, Q. F., Tipping, A. J., Datta, K., Mittal, R., Goldson, A. J., Sexton, D. W. and Holmes, C. C. (2013). Methods for qPCR gene expression profiling applied to 1440 lymphoblastoid single cells. *Methods* **59**, 71-79. doi:10.1016/j.ymeth.2012.10.004

Luong, M. X., Van Der Meijden, C. M., Xing, D. X., Hesselton, R., Monuki, E. S., Jones, S. N., Lian, J. B., Stein, J. L., Stein, G. S., Neufeld, E. J. et al. (2002). Genetic ablation of the CDP/Cux protein C terminus results in hair cycle defects and reduced male fertility. *Mol. Cell. Biol.* **22**, 1424-1437. doi:10.1128/MCB.22.5.1424-1437.2002

Mao, Q., Stinnett, H. K. and Ho, R. K. (2015). Asymmetric cell convergence-driven zebrafish fin bud initiation and pre-pattern requires Tbx5a control of a mesenchymal Fgf signal. *Development* **142**, 4329-4339. doi:10.1242/dev.124750

Marsman, J., O'neill, A. C., Kao, B. R.-Y., Rhodes, J. M., Meier, M., Antony, J., Mönnich, M. and Horsfield, J. A. (2014). Cohesin and CTCF differentially regulate spatiotemporal runx1 expression during zebrafish development. *Biochim. Biophys. Acta* **1839**, 50-61. doi:10.1016/j.bbagrm.2013.11.007

Matsumoto, K., Nishihara, S., Kamimura, M., Shiraishi, T., Otoguro, T., Uehara, M., Maeda, Y., Ogura, K., Lumsden, A. and Ogura, T. (2004). The prepattern transcription factor Irx2, a target of the FGF8/MAP kinase cascade, is involved in cerebellum formation. *Nat. Neurosci.* **7**, 605-612. doi:10.1038/nn1249

Mendoza, M., Norden, C., Durrer, K., Rauter, H., Uhlmann, F. and Barral, Y. (2009). A mechanism for chromosome segregation sensing by the NoCut checkpoint. *Nat. Cell Biol.* **11**, 477-483. doi:10.1038/ncb1855

Mercader, N., Leonardo, E., Azpiazu, N., Serrano, A., Morata, G., Martínez, C. and Torres, M. (1999). Conserved regulation of proximodistal limb axis development by Meis1/Hth. *Nature* **402**, 425-429. doi:10.1038/46580

Minina, E. A., Reza, S. H., Gutierrez-Beltran, E., Elander, P. H., Bozhkov, P. V. and Moschou, P. N. (2017). The Arabidopsis homolog of Scc4/MAU2 is essential for embryogenesis. *J. Cell Sci.* **130**, 1051-1063. doi:10.1242/jcs.196865

Mishiro, T., Ishihara, K., Hino, S., Tsutsumi, S., Aburatani, H., Shirahige, K., Kinoshita, Y. and Nakao, M. (2009). Architectural roles of multiple chromatin insulators at the human apolipoprotein gene cluster. *EMBO J.* **28**, 1234-1245. doi:10.1038/emboj.2009.81

Misulovin, Z., Pherson, M., Gause, M. and Dorsett, D. (2018). Brca2, Pds5 and Wapl differentially control cohesin chromosome association and function. *PLoS Genet.* **14**, e1007225. doi:10.1371/journal.pgen.1007225

Mo, R., Freer, A. M., Zinyk, D. L., Crackower, M. A., Michaud, J., Heng, H. H., Chik, K. W., Shi, X. M., Tsui, L. C., Cheng, S. H. et al. (1997). Specific and redundant functions of Gli2 and Gli3 zinc finger genes in skeletal patterning and development. *Development* **124**, 113-123.

Mohan, K., Iglesias, P. A. and Robinson, D. N. (2012). Separation anxiety: stress, tension and cytokinesis. *Exp. Cell Res.* **318**, 1428-1434. doi:10.1016/j.yexcr.2012.03.028

Morales, C. and Losada, A. (2018). Establishing and dissolving cohesion during the vertebrate cell cycle. *Curr. Opin. Cell Biol.* **52**, 51-57. doi:10.1016/j.ceb.2018.01.010

Mouri, K., Horiuchi, S.-Y. and Uemura, T. (2012). Cohesin controls planar cell polarity by regulating the level of the seven-pass transmembrane cadherin Flamingo. *Genes Cells* **17**, 509-524. doi:10.1111/j.1365-2443.2012.01604.x

Muto, A., Ikeda, S., Lopez-Burks, M. E., Kikuchi, Y., Calof, A. L., Lander, A. D. and Schilling, T. F. (2014). Nipbl and mediator cooperatively regulate gene expression to control limb development. *PLoS Genet.* **10**, e1004671. doi:10.1371/journal.pgen.1004671

Pal, R., Ramdzan, Z. M., Kaur, S., Duquette, P. M., Marcotte, R., Leduy, L., Davoudi, S., Lamarche-Vane, N., Iulianella, A. and Nepveu, A. (2015). CUX2

protein functions as an accessory factor in the repair of oxidative DNA damage. *J. Biol. Chem.* **290**, 22520-22531. doi:10.1074/jbc.M115.651042

Peters, J.-M. and Nishiyama, T. (2012). Sister chromatid cohesion. *Cold Spring Harb. Perspect. Biol.* **4**, a011130. doi:10.1101/cshperspect.a011130

Pfeiffer, R. A. and Correll, J. (1993). Hemimelia in Brachmann-de Lange syndrome (BDLS): a patient with severe deficiency of the upper and lower limbs. *Am. J. Med. Genet.* **47**, 1014-1017. doi:10.1002/ajmg.1320470715

Ramdzan, Z. M., Vadnais, C., Pal, R., Vandal, G., Cadieux, C., Leduy, L., Davoudi, S., Hulea, L., Yao, L., Karnezis, A. N. et al. (2014). RAS transformation requires CUX1-dependent repair of oxidative DNA damage. *PLoS Biol.* **12**, e1001807. doi:10.1371/journal.pbio.1001807

Ramdzan, Z. M., Pal, R., Kaur, S., Leduy, L., Bérubé, G., Davoudi, S., Vadnais, C. and Nepveu, A. (2015). The function of CUX1 in oxidative DNA damage repair is needed to prevent premature senescence of mouse embryo fibroblasts. *Oncotarget* **6**, 3613-3626. doi:10.18632/oncotarget.2919

Raspopovic, J., Marcon, L., Russo, L. and Sharpe, J. (2014). Modeling digits. Digit patterning is controlled by a Bmp-Sox9-Wnt Turing network modulated by morphogen gradients. *Science* **345**, 566-570. doi:10.1126/science.1252960

Remeseiro, S., Cuadrado, A., Carretero, M., Martínez, P., Drosopoulos, W. C., Cañamero, M., Schildkraut, C. L., Blasco, M. A. and Losada, A. (2012). Cohesin-SA1 deficiency drives aneuploidy and tumourigenesis in mice due to impaired replication of telomeres. *EMBO J.* **31**, 2076-2089. doi:10.1038/emboj.2012.11

Robinson, M. D., Mccarthy, D. J. and Smyth, G. K. (2010). edgeR: a bioconductor package for differential expression analysis of digital gene expression data. *Bioinformatics* **26**, 139-140. doi:10.1093/bioinformatics/btp616

Roux, K. J., Kim, D. I., Raida, M. and Burke, B. (2012). A promiscuous biotin ligase fusion protein identifies proximal and interacting proteins in mammalian cells. *J. Cell Biol.* **196**, 801-810. doi:10.1083/jcb.201112098

Sansregret, L., Vadnais, C., Livingstone, J., Kwiatkowski, N., Awan, A., Cadieux, C., Leduy, L., Hallett, M. T. and Nepveu, A. (2011). Cut homeobox 1 causes chromosomal instability by promoting bipolar division after cytokinesis failure. *Proc. Natl. Acad. Sci. USA* **108**, 1949-1954. doi:10.1073/pnas.1008403108

Seipold, S., Priller, F. C., Goldsmith, P., Harris, W. A., Baier, H. and Abdelilah-Seyfried, S. (2009). Non-SMC condensin I complex proteins control chromosome segregation and survival of proliferating cells in the zebrafish neural retina. *BMC Dev. Biol.* **9**, 40. doi:10.1186/1471-213X-9-40

Skibbens, R. V. (2008). Mechanisms of sister chromatid pairing. *Int. Rev. Cell Mol. Biol.* **269**, 283-339. doi:10.1016/S1937-6448(08)01005-8

Smemo, S., Tena, J. J., Kim, K.-H., Gamazon, E. R., Sakabe, N. J., Gómez-Marín, C., Aneas, I., Credidio, F. L., Sobreira, D. R., Wasserman, N. F. et al. (2014). Obesity-associated variants within FTO form long-range functional connections with IRX3. *Nature* **507**, 371-375. doi:10.1038/nature13138

Smith, T. G., Laval, S., Chen, F., Rock, M. J., Strachan, T. and Peters, H. (2014). Neural crest cell-specific inactivation of Nipbl or Mau2 during mouse development results in a late onset of craniofacial defects. *Genesis* **52**, 687-694. doi:10.1002/dvg.22780

Snippert, H. J., Van Der Flier, L. G., Sato, T., Van Es, J. H., Van Den Born, M., Kroon-Veenboer, C., Barker, N., Klein, A. M., Van Rheenen, J., Simons, B. D. et al. (2010). Intestinal crypt homeostasis results from neutral competition between symmetrically dividing Lgr5 stem cells. *Cell* **143**, 134-144. doi:10.1016/j.cell.2010.09.016

Song, A. T., Galli, A., Leclerc, S., Nattel, S., Mandato, C. and Andelfinger, G. (2017). Characterization of Sgo1 expression in developing and adult mouse. *Gene Expr. Patterns* **25-26**, 36-45. doi:10.1016/j.gep.2017.04.004

Sumara, I., Vorlaufer, E., Gieffers, C., Peters, B. H. and Peters, J.-M. (2000). Characterization of vertebrate cohesin complexes and their regulation in prophase. *J. Cell Biol.* **151**, 749-762. doi:10.1083/jcb.151.4.749

Tao, H., Kawakami, Y., Hui, C.-C. and Hopyan, S. (2017). The two domain hypothesis of limb prepattern and its relevance to congenital limb anomalies. *Wiley Interdiscip. Rev. Dev. Biol.* **6**, e270. doi:10.1002/wdev.270

Tao, H., Zhu, M., Lau, K., Whitley, O. K. W., Samani, M., Xiao, X., Chen, X. X., Hahn, N. A., Liu, W., Valencia, M. et al. (2019). Oscillatory cortical forces promote three dimensional cell intercalations that shape the murine mandibular arch. *Nat. Commun.* **10**, 1703. doi:10.1038/s41467-019-09540-z

Te Welscher, P., Fernandez-Teran, M., Ros, M. A. and Zeller, R. (2002). Mutual genetic antagonism involving GLI3 and dHAND prepatterns the vertebrate limb bud mesenchyme prior to SHH signaling. *Genes Dev.* **16**, 421-426. doi:10.1101/gad.219202

Tedeschi, A., Wutz, G., Huet, S., Jaritz, M., Wuensche, A., Schirghuber, E., Davidson, I. F., Tang, W., Cisneros, D. A., Bhaskara, V. et al. (2013). Wapl is an essential regulator of chromatin structure and chromosome segregation. *Nature* **501**, 564-568. doi:10.1038/nature12471

Teo, G., Liu, G., Zhang, J., Nesvizhskii, A. I., Gingras, A.-C. and Choi, H. (2014). SAINTexpress: improvements and additional features in significance analysis of INTeractome software. *J. Proteomics* **100**, 37-43. doi:10.1016/j.jprot.2013.10.023

Waizenegger, I. C., Hauf, S., Meinke, A. and Peters, J.-M. (2000). Two distinct pathways remove mammalian cohesin from chromosome arms in prophase and from centromeres in anaphase. *Cell* **103**, 399-410. doi:10.1016/S0092-8674(00)00132-X

Warde-Farley, D., Donaldson, S. L., Comes, O., Zuberi, K., Badrawi, R., Chao, P., Franz, M., Grouios, C., Kazi, F., Lopes, C. T. et al. (2010). The GeneMANIA prediction server: biological network integration for gene prioritization and predicting gene function. *Nucleic Acids Res.* **38**, W214-W220. doi:10.1093/nar/gkq537

Wong, M. D., Dazai, J., Walls, J. R., Gale, N. W. and Henkelman, R. M. (2013). Design and implementation of a custom built optical projection tomography system. *PLoS ONE* **8**, e73491. doi:10.1371/journal.pone.0073491

Woolley, T. E., Baker, R. E., Tickle, C., Maini, P. K. and Towers, M. (2014). Mathematical modelling of digit specification by a sonic hedgehog gradient. *Dev. Dyn.* **243**, 290-298. doi:10.1002/dvdy.24068

Wyngaarden, L. A., Vogeli, K. M., Ciruna, B. G., Wells, M., Hadjantonakis, A.-K. and Hopyan, S. (2010). Oriented cell motility and division underlie early limb bud morphogenesis. *Development* **137**, 2551-2558. doi:10.1242/dev.046987

Xu, B., Sowa, N., Cardenas, M. E. and Gerton, J. L. (2015). L-leucine partially rescues translational and developmental defects associated with zebrafish models of Cornelia de Lange syndrome. *Hum. Mol. Genet.* **24**, 1540-1555. doi:10.1093/hmg/ddu565

Yan, J., Enge, M., Whitington, T., Dave, K., Liu, J., Sur, I., Schmierer, B., Jolma, A., Kivioja, T., Taipale, M. et al. (2013). Transcription factor binding in human cells occurs in dense clusters formed around cohesin anchor sites. *Cell* **154**, 801-813. doi:10.1016/j.cell.2013.07.034

Zhang, S.-S., Kim, K.-H., Rosen, A., Smyth, J. W., Sakuma, R., Delgado-Olguin, P., Davis, M., Chi, N. C., Puviindran, V., Gaborit, N. et al. (2011). Iroquois homeobox gene 3 establishes fast conduction in the cardiac His-Purkinje network. *Proc. Natl. Acad. Sci. USA* **108**, 13576-13581. doi:10.1073/pnas.1106911108

Zhulyn, O., Li, D., Deimling, S., Vakili, N. A., Mo, R., Puviindran, V., Chen, M.-H., Chuang, P.-T., Hopyan, S. and Hui, C.-C. (2014). A switch from low to high Shh activity regulates establishment of limb progenitors and signaling centers. *Dev. Cell* **29**, 241-249. doi:10.1016/j.devcel.2014.03.002